UNIVERSIDAD DE GRANADA

FACULTAD DE CIENCIAS

Departamento de Electrónica

y Tecnología de Computadores

MODELADO DE MECANISMOS FÍSICOS Y LAS ESTRUCTURAS CONSTITUYENTES DE UN TRANSISTOR DE EFECTO CAMPO ORGÁNICO

TESIS DOCTORAL

Pablo Lara Bullejos

2009

Editor: Editorial de la Universidad de Granada
Autor: Pablo Lara Bullejos
D.L.: GR. 3520-2009
ISBN: 978-84-692-6400-3

UNIVERSIDAD DE GRANADA

FACULTAD DE CIENCIAS

Departamento de Electrónica

y Tecnología de Computadores

MODELADO DE MECANISMOS FÍSICOS Y LAS ESTRUCTURAS CONSTITUYENTES DE UN TRANSISTOR DE EFECTO CAMPO ORGÁNICO

Tesis Doctoral presentada por:

Pablo Lara Bullejos

para optar al grado de doctor en Ingeniería Electrónica

Granada, 22 de Junio de 2009

Fdo. Pablo Lara Bullejos

Departamento de Electrónica
y Tecnología de Computadores

Dr. Juan Antonio Jiménez Tejada, Profesor Titular y Catedrático del Departamento de Electrónica y Tecnología de Computadores de la Universidad de Granada.
Dr. M. Jamal Deen, Profesor y Catedrático de Investigación en la Universidad de McMaster, Hamilton (Ontario) Canada.

CERTIFICAN:

Que el trabajo de investigación que se recoge en la presente Memoria, titulada *MODELADO DE MECANISMOS FÍSICOS Y LAS ESTRUCTURAS CONSTITUYENTES DE UN TRANSISTOR DE EFECTO CAMPO ORGÁNICO*, presentada por **D. Pablo Lara Bullejos** para optar al grado de Doctor en Ingeniería Electrónica, ha sido realizado en su totalidad bajo su dirección en el Departamento de Electrónica y Tecnología de Computadores de la Universidad de Granada así como en el departamento Electrical and Computing Engineering de la facultad de Ingeniería de la Universidad de McMaster, Hamilton (Ontario) Canada.

Granada, 22 de Junio, 2009

MODELLING OF PHYSICAL MECHANISMS IN ORGANIC THIN FILM TRANSISTORS AND RELATED STRUCTURES.

By

Pablo Lara Bullejos

A Thesis

Submitted to the Graduate School

of the University of Granada

in Partial Fulfillment of the Requirements

for the Degree of

Doctor of Philosophy

University of Granada

DOCTORATE PROGRAM(2009) UNIVERSITY OF GRANADA

(Departamento de Electrónica y Tecnología

de Computadores) Granada, Spain.

TITLE: Modelling of Physical Mechanisms in Organic Thin Film Transistors and Related Structures.

Author: Pablo **Lara Bullejos**

Master degree in Electronic Engineering (University of Granada)

Supervisors: Juan Antonio Jiménez Tejada
Professor, Departamento de Electrónica y Tecnología de Computadores,
(University of Granada, Spain)
M. Jamal Deen
Professor and Senior Canada Research Chair,
Department of Electrical and Computer Engineering,
(McMaster University, Canada)

NUMBER OF PAGES: vii, 103

Abstract

In modern organic semiconductor devices, the performance of the device is limited by non-idealities which are not characterized by traditional models of transport. A physical model that includes several transport mechanisms suited to organic devices is proposed in this thesis. These physical mechanisms are charge injection (thermionic and tunnelling), charge creation at metal-organic interface (electrochemically), and charge transport through the organic layer (charge drift and space charge effects).

Organic diodes and organic thin film transistors have been studied using the proposed model to obtain a better understanding of the physical and electrochemical phenomena that determine their performance characteristics. The dependence of the current with the applied voltage and temperature through these organic semiconductor devices, have been carefully reviewed and comparisons between predictions from the proposed models and experiments studied. These comparisons validate the models by showing the good agreement between experimental data with model calculations for both organic semiconductor diodes and thin-film transistors.

Acknowledgement

I would like to thank my supervisors, Dr. Juan Antonio Jiménez Tejada and Dr. M. Jamal Deen for their support, encouragement and guidance throughout my time at the University of Granada and McMaster University. They spent a lot of their valuable time together with me, and shared their vast experience in modelling and characterization with me. Without them, none of the research work could be possible. I would like to thank my co-workers for their constant support and inspiration, Ognian Marinov, Ross Datars, Francisco Manuel Gómez, Salvador Rodríguez, Juan Antonio Lopez, Juan Enrique Carceller, Noel Rodríguez, Carlos Sampedro, Luca Donetti, Francisco Javier Ruiz and Francisco Jimenez. I will cherish the time with them forever.

Finally, I would like to thank my wife, thank you for your love and support throughout my life.

Table of Contents

Chapter 1:
Introduction and Background

1.1 Introduction

The objective of this thesis is to contribute to the theoretical modelling of the injection and transport processes in organic and polymeric thin-film transistors (hereafter, we use organic to mean both organic and polymeric). Organic thin-film transistor (OTFTs) refers to field-effect transistors which use molecular semiconductors based on carbon chains. The technology of OTFTs have advantages over crystalline, polycrystalline and amorphous silicon processes. Important advantages of OTFTs are the low-cost processing and the possible use in flexible substrates. These advantages make OTFTs attractive to applications like electronic tags or drivers in active matrix displays [1.1], [1.2], [1.3]. Because of its advantages and possibilities for applications, OTFTs are being actively researched and developed by both researchers and in companies for commercial applications.

A main disadvantage is the low carrier mobility found in organic materials. A lot of effort has been directed to increase the mobilities in OTFTs [1.3]. However, the performance of these devices still suffers from other limitations that have limited their commercial applications. Some of these problems in OTFTs are the presence of non-ohmic contacts, the non-repeatability of the parameters, the non-stationary effects or the dependence of the mobility on the organic film thickness [1.4], and [1.5].

As a response to the cited problems, this thesis is devoted to address the contact effects in OTFTs as well as to bring the theory of charge transport closer to the experiments. Considering that the same principles for the contact effects in organic diodes are valid for OTFTs [], organic diodes are studied in a first step. Then, we focus on the study of contact effects in OTFTs.

In this introductory chapter, we summarize the steps that have been followed in this study of organic diodes and OTFTs, pointing out some of the key references used. The structure of the thesis is detailed in Section 1.2. We also introduce the basis of the conduction in organic semiconductors in Section 1.3 with the objective of making an easy reading for those who are not familiar with the field of organic electronics.

1.2 Thesis Structure

As mentioned above, the objective of this thesis is to address the contact effects in OTFTs. Previous experience in contacts of inorganic devices [1.7], [1.8], [1.9] supports our study in organic devices. This work is also supported by previous works concerning organic electronics. In particular, electrical characteristics in different OTFTs were analyzed [1.10], [1.11], and well-known theories of charge transport [1.12], [1.13] and contact effects in OTFTs [1.14], [1.15] are discussed in this work.

The nucleus of this thesis is a model that combines different physical and chemical mechanisms that take place in organic diodes and at the contacts of OTFTs. This model has been proposed after a careful review of the results reported in the literature. The results of this thesis have been shared to the scientific community in published papers [1.16], [1.17] and oral presentations [1.18], [1.19], [1.20], [1.21], [1.22], in order to provide a feedback to device designers and technologists.

This work is divided in three main chapters plus introducing and concluding chapters. In the second chapter, a unified model for charge injection and transport in

rganic diodes is presented. Although contact effects in OTFTs are our major objective, an initial study of the processes in monolayer diodes is very valuable, especially because the same phenomena are present in both types of devices [1.6]. At the same time, we can avoid extra problems like the extraction of contact effects in OTFTs [1.4]. Subsequently, results from the study of diodes are applied to OTFTs in chapters 3 and 4.

In the second chapter, a special interest is placed on charge injection from the contacts. Existing models, such as thermionic emission and tunnel injection, are combined with effects associated with oxidation/reduction reactions at the electrodes. Charges are formed at the electrodes by oxidation or reduction in a process governed by the Nernst equation, and these charges modulate the injection barrier. A current-voltage relationship for organic or polymeric diodes that incorporates these injection phenomena, as well as the charge transport by the drift mechanism is presented and discussed. The voltage ranges in which these effects are dominant are estimated. As a result of the first part of this work, current-voltage and current-temperature relations are obtained and they are used to explain published experimental data in diodes.

In the third chapter of this work, the study in diodes is applied to the contacts of OTFTs. In OTFTs, the flow of charge is limited not only by drift in the organic film, but also by the effects of the contacts formed between the organic layer and source/drain electrodes. A compact model, partly based on the work in diodes, is proposed to study the electrical characteristics of the contacts in OTFTs. The model reproduces and explains several features that have been reported for current-voltage curves, I_D-V_C, at the contacts of OTFTs. As a separate section in the third chapter, we highlight the difficulties of extracting I_D-V_C curves [1.3], [1.4], [1.5] in OTFTs. We review the assumptions of a widely used extraction technique based on measuring transistors of different channel lengths [1.5]. We also propose a method for the extraction of I_D-V_C

curves and mobilities when a set of transistors with different channel lengths is not available.

In the fourth chapter of the thesis, a physical model is proposed and compared to the compact model proposed in chapter 3. The physical model is accompanied with a procedure to evaluate the charge density in the low conductivity region located between the metal and the accumulated intrinsic channel of OTFTs. This procedure is based on the results obtained in the previous two chapters. A key issue, such as the dependence of the current flowing across the contacts with the voltage and the temperature, is treated in transistors with different metal-organic barriers. The interpretation of current-voltage and current-temperature curves at the contacts of organic transistors lies at the heart of the work developed in this thesis: the interrelation of different physical phenomena (the injection of carriers through the barrier at the metal-organic interface, the modulation of that barrier by reduction-oxidation reactions and the drift of charge in the bulk of the contact).

The fifth chapter ends this work with the final conclusions and recommendations for future work.

1.3 Organic Materials.

Solid-state physics can be divided according to three different classes of molecules, conductors, insulators and semiconductors. Insulators have a large band gap (or forbidden energy gap) that prevents electrons from the occupied valence band transferring to the outer conduction band, which is unoccupied.

The semiconductors refer to the II-VI, III-V and IV-groups in the periodic system. These materials possess a smaller energy gap, making them more conductive. Carbon (C) belongs to the group IV class of semiconductor materials; however it has

traditionally behaved as an insulator. In spite of this natural behavior of carbon, conduction was discovered in carbon materials, polyacetylene particularly [1.23], in 1977. In addition to this discovery, the group of Tang and Van Slyke at Eastman-Kodak presented luminescence from an organic material in 1987 [1.24].

These dates can be considered as the dawn of a new era in the semiconductor technology, the era of the organic devices. An overview of the basic principles of conduction in organic semiconductors is done in next subsections: the structure of the organic molecules, the structure of an organic solid, and finally a hopping model for the transfer of charge between molecules are reviewed.

1.3.1 Structure of the Molecules.

In organic molecules, the electrons are distributed in orbitals around the core of the carbon atoms according to their electron probability functions. The outermost electron orbitals of different atoms interact and link these atoms, forming molecules that strive for the lowest energy as possible. A bond to another atom contributes to a lower energy of the system and the maximal amount of bonds to adjacent atoms is therefore desired. An organic semiconductor molecule contains a backbone of carbon atoms, (Fig. 1.1c), and a certain number of functional groups that are attached to it. The backbone of the organic materials is made up of strongly localised bonds between the carbon atoms, its conductivity is enabled through the bonds between the orbitals that are orthogonal to the backbone (p-orbitals). Therefore, two different kinds of bonds can be considered.

When the orbitals for the electrons overlap in a formation of a symmetrical rotational orbital around its bond axis, a σ- bond could be considered (Fig. 1.1a). An overlap with the absence of rotational symmetry could be considered as a π- bond, (Fig. 1.1a). The bonds are formed through the overlap of the electron orbitals where a large

overlap is a strong bonding, which also is the case for σ- bonds. Also, note that π- bonds are a requirement for double bond between two atoms.

The overlap between the adjacent electron orbitals is increased with the presence of π-bonds. This contributes to an overlap between orbitals in the whole or the main part of the molecule; the orbitals are considered delocalised. The delocalisation of the π-bonds along the boundary of the molecule results in a very stable state and enables the mobility of charges through the molecule, (Figs. 1.1c-1.1d). The electrons can move within the molecule via π-electron cloud where they do not belong to a single bond or atom, but rather a group.

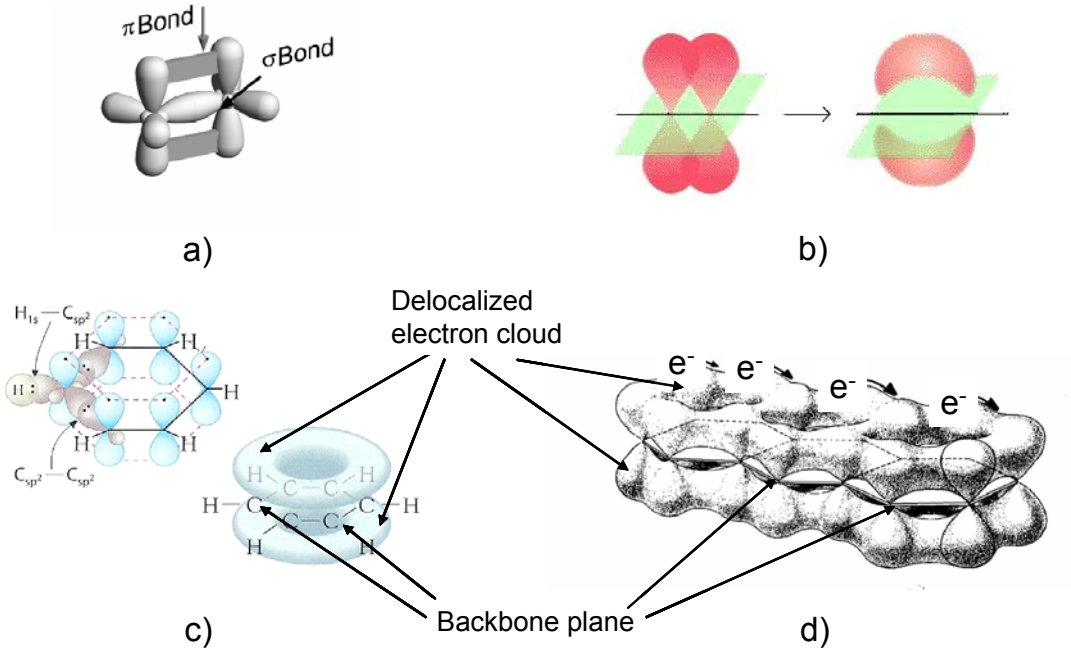

Figure 1.1. (a) Different kinds of bond attending to the rotational symmetry. (b) Formation of a π-bond from the overlapping of two p-orbitals between two carbon atoms. (c) Formation of six delocalized π-bonds in the molecule of the benzene. (d) Electron cloud in the molecule anthracene.

To end this subsection, we would like to introduce two different classes of materials, organic and polymeric semiconductors, which are fabricated by different processes, although they show very similar electrical characteristics. The difference between these two types is in the conjugation length, which is defined as the length

where the electrons are free to move within the structure. Polymeric semiconductors are formed by a long repeating chain of similar smaller molecules, called monomers, and so they tend to have long conjugation length, while organic, or small molecules, have a shorter one. The most commonly used material with the most explored properties among the small molecules is hydroxyquinoline aluminium (Alq3). A frequently used conjugated polymer is the poly paraphenylene vinylene (PPV).

1.3.2 Electronic Structure of Organic Solids.

In spite of the good conduction within the molecule, due to the formation of a π-electron cloud, the organic semiconductors are formed by a system of molecules and the macroscopic conduction depends not only on the motion of charge within the molecule but also on the transfer of charge between molecules. In this subsection, we review the distribution of electrons in an organic solid formed by many molecules.

In organic solids, the molecules are held together by weak physical bonding, (Van der Waals forces), resulting in an arragement of molecules where each molecule has full shells and stable electronic configuration. In this case, the electrons are distributed around the core of the molecules they belong to. The transfer of charges between molecules is not as easy as in a covalent crystal where the electrons are not localized around the nucleus, but are in certain directions forming the bonds. This difference between the molecular crystal in organic semiconductors and the covalent crystal in inorganic semiconductors is represented in Fig. 1.2. The energetic diagram of organic crystals is described below.

The electronic structure of a polyatomic molecule is shown in Fig. 1.3a The effective potential well of an electron is formed by the atomic nuclei and other electrons. The wells of the nuclei are merged in the upper part to form a broad well.

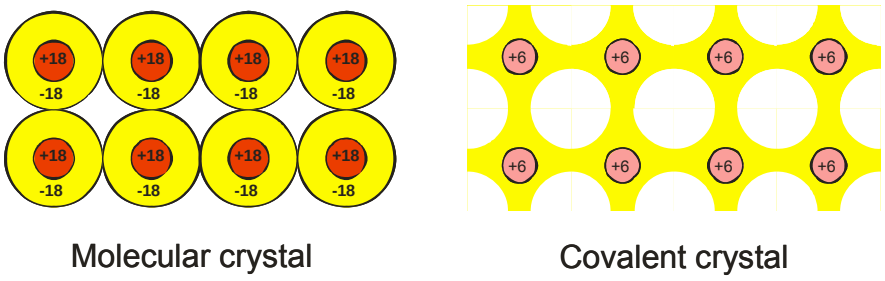

Figure 1.2. (a) In molecular crystals, the electrons are distributed around the core of the molecules they belong to. The charges find a barrier which prevents the transferring between molecules. (b) The electrons are distributed along the crystal forming bonds. The band transport is valid and any extra electron would be free to move through to this lattice.

Deep atomic orbitals are still localized in the atomic potential well (core levels), but the upper atomic orbitals interact to form delocalized molecular orbitals.

When molecules come together to form an organic solid, the electronic structure becomes like in Fig. 1.3b. Since the molecules interact only by weak van der Waals forces, the highest occupied molecular orbital (HOMO) and the lowest unoccupied molecular orbital (LUMO) are usually localized in each molecule. Thus, the electronic structure of an organic solid largely preserves that of a molecule, and the validity of the band theory is open to debate [1.25]. A better approach for the conduction in organic semiconductors is the charge transport via hopping over the barriers between molecules [1.12]. This will be briefly reviewed in the next subsection.

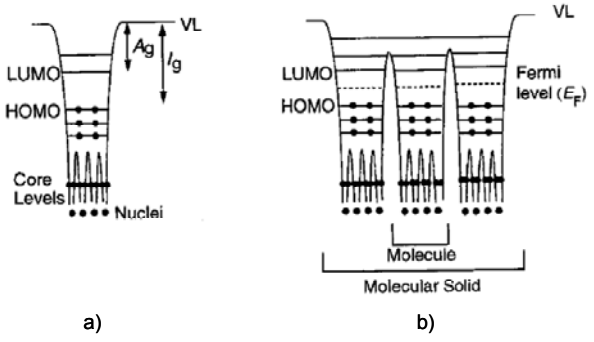

Figure 1.3. Electronic structure represented with potential wells (a) Polyatomic molecule (b) Organic solid.

1.3.3 Conduction in Organic Semiconductors

An important conclusion from the previous subsection is that the transport through organic materials is limited by the transfer of charges between the molecules. An energy barrier is present between the molecules (Fig. 1.3b), and the closer the molecules, the better the conduction. The mobility is therefore a result of significant orbital overlap among the molecules, and the larger the overlap, the larger the mobility of the material [1.26], [1.27], [1.28].

As mentioned in the previous subsection, it is generally agreed that charge transport in organic semiconductors occurs via hopping of self-trapped polarons. Evidence for hopping transport mostly relies on the fact that the field-effect mobility of organic semiconductors is thermally activated [1.15], [1.27]. By comparison, the carrier mobility of highly pure organic single crystals, obtained by time of flight measurements, is temperature dependent, suggesting band-type transport. However, the corresponding mean free path remains lower than the lattice parameters and therefore contradicts such a transport process [1.25].

The picture given above for the conduction in organic semiconductors is a first-order approximation. Contact effects, charge build up, non-repeatability of the parameters and non-stationarity, are second-order effects to take into account when modelling the conduction of organic semiconductors [1.4]. The hopping transport, briefly mentioned above, can be combined with other approaches to explain experimental data [1.29], as it is done in the present thesis.

References

1.1. M. J. Deen, M. H. Kazemeini, S. Holdcroft, "Contact effects and extraction of intrinsic parameters in poly(3-alkylthiophene) thin film field-effect transistors", *J. Appl. Phys.*, vol. 103(124509), pp. 1–7, (2008).

1.2. B. H. Hamadani, D. Natelson, "Gated nonlinear transport in organic polymer field effect transistors", *J. Appl. Phys*., vol. 95, pp. 1227–1232, (2004).

1.3. L. Bürgi, T.J. Richards, R.H. Friend, H. Sirringhaus, "Close look at charge carrier injection in polymer field effect transistors", *J. Appl. Phys*., vol. 94(9), pp. 6129–6137, (2003).

1.4. O. Marinov, M. J. Deen, B. Iniguez, "Charge Transport in Organic and Polymer Thin-Film Transistors: Recent Issues", *IEE Proc.-Circuits Devices and Syst.*, vol. 152(3), pp. 189–209, (2005).

1.5. B. H. Hamadani, D. Natelson, "Extracting contact effects in organic FETs", *Proc. of the IEEE.*, vol. 93(7), pp. 1306–1311, (2005).

1.6. R. A. Street, A. Salleo, "Contact effects in polymer transistors", *Appl. Phys. Lett.*, vol. 81(15), pp. 2887–2889, (2002).

1.7. J. A. Jiménez Tejada, P. Lara Bullejos, J. A. López Villanueva, F.M. Gómez-Campos, S. Rodríguez-Bolívar, and J. E. Carceller, *Proc. 7th Eur. Workshop on Low Temperature Electronics*, pp. 5-10, (2006).

1.8. J. A. Jiménez Tejada, P. Lara Bullejos, J. A. López Villanueva, F.M. Gómez-Campos, S. Rodríguez-Bolívar, and M. Jamal Deen, "Determination of the concentration of recombination centers in thin asymmetrical *p-n* junctions from capacitance transient spectroscopy", *Appl. Phys. Lett.*, vol. 89(112107), pp. 1-3, (2006).

1.9. J. A. Jiménez Tejada, M. J. Deen, P. Lara Bullejos, J. A. López Villanueva, F.M. Gómez-Campos, and S. Rodríguez-Bolívar, *IEEE Conference Proceeding Spanish Conference on Electron Devices*, (2007).

1.10. Z. Xie, M. S. Abdou, A. Lu, M. J. Deen and S. Holdcroft, "Electrical Characteristics of Poly(3-Hexylthiophene) Thin Film MISFETs", *Can. J. Phys.*, vol. 70, pp. 1171-1177, (1992).

1.11. M. J. Deen, M. H. Kazemeini, Y. M. Haddara, J. Yu, G. Vamvounis, S. Holdcroft, and W. Woods, "Electrical Characterization of Polymer-Based FETs Fabricated by Spin-Coating Poly(3-alkylthiophene)s", *IEEE Trans. Electron Devices.,* vol. 51, pp. 1892 (2004).

1.12. V.I. Arkhipov, E. V. Emelianova, Y.H. Tak, H. Bassler, "Charge injection into light emitting diodes: theory and experiment", *J. Appl. Phys.*, vol. 84(2), pp. 848–856, (1998).

1.13. N. F. Mott and R. W. Gurney, *Electronic Processes in Ionic Crystals,* Clarendon Oxford 1940.

1.14. B. Hamadani, D. Natelson, "Temperature dependent contact resistances in high quality polymer field effect transistors", *Appl. Phys.Lett.*, vol. 84(3), pp. 443–445, (2004).

1.15. B. H. Hamadani, D. Natelson, "Nonlinear charge injection in organic field-effect transistors", *J. Appl. Phys.*, vol. 97(064508), pp. 1–7, (2005).

1.16. P. Lara Bullejos, J. A. Jiménez Tejada, M. J. Deen, O. Marinov, and W. R. Datars, "Unified model for the injection and transport of charge in organic diodes", *J. Appl. Phys.,* 103(064504), 1-12 (2008).

1.17. P. Lara Bullejos, J. A. Jiménez Tejada, S. Rodríguez-Bolívar, M. J. Deen, and O. Marinov, "Model for the injection of charge through the contacts of organic transistors", *J. Appl. Phys.*, vol. 105(084516), pp. 1–8, (2009).

1.18. J. A. Jiménez Tejada, P. Lara Bullejos, M. J. Deen, and W. Datars, *Proc. IEEE Electrochemical Society Meeting (212th ECS)* Washington DC (2007).

1.19. P. Lara Bullejos, J. A. Jiménez Tejada, M. J. Deen, O. Marinov and S. Rodríguez-Bolívar, *Proc. IEEE International Symposium on Flexible Electronics (ISFE 08)* Tarragona Spain (2008).

1.20. J. A. Jiménez Tejada, P. Lara Bullejos, and M. J. Deen, *Proc. IEEE International Workshop on Compact Thin-Film Transistor Modeling for Circuit Simulation*, Cambridge U. K. (2008).

1.21. P. Lara Bullejos, J. A. Jiménez Tejada, M. J. Deen, O. Marinov, and S. Rodríguez-Bolívar, *IEEE Proc. Spanish Conference on Electron Devices,* Santiago de Compostela, Spain (2009).

1.22. P. Lara Bullejos, J. A. Jiménez Tejada, M. J. Deen, and O. Marinov, *Proc. IEEE Electrochemical Society Meeting (216th ECS)* Wien (2009). In press.

1.23. C. K. Chiang, C. R. Fincher Jr., Y. W. Park, A. J. Heeger, H. Shirakawa, E. J. Louis, S. C. Gau, and A. G. MacDiarmid, "Electrical Conductivity in Doped Polyacetylene", *Phys. Rev. Lett.,* Vol. 39, *pp.* 1098, (1977).

1.24. C. W. Tang, S. A. Van Slyke, "Organic Electroluminscent Diodes", *Appl. Phys. Lett.*, vol. 51, pp. 913, (1987).

1.25. Karl, N., "Charge carrier transport in organic semiconductors", *Synth. Met.*, 133-134, pp. 649–657 (2003).

1.26. D. D. Schroepfer and P. P. Ruden, "Hydrostatic pressure effects on poly(3-hexylthiophene", *Appl. Phys. Lett.*, vol. 92(013305), pp. 1-3 (2008).

1.27. Martens, H.C.F., Blom, P.W.M., and Schoo, H.F.M., "Comparative study of hole transport in poly(p-phenylene vinylene) derivatives", *Phys. Rev. B*, vol. 61(11), pp. 7489–7493 (2000).

1.28. R. A. Street, J. E. Northrup, and A. Salleo, "Transport in polycrystalline polymer thin-film transistors", *Phys. Rev. B*, vol. 71(165202), pp. 1–13 (2005).

1.29. R. Agrawal, P. Kumar, S. Ghosh and A. K. Mahapatro, "Thickness dependence of space charge limited current and injection limited current in organic molecular semiconductors", *Appl. Phys. Lett. B*, vol. 93(073311), pp. 1–3 (2008).

Chapter 2:
Injection and Transport of Charge in Organic Diodes

2.1 Introduction

The importance of studying the charge injection and transport in organic diodes and transistors has recently been critically reviewed in [2.1]. Studies by different authors [2.2], [2.3], in diodes with similar contact materials, as for example the contact between indium-tin-oxide (ITO) and poly(2-methoxy,5-(2'-ethyl-hexoxy)-1,4-phenylene-vinylene) MEH-PPV, have shown both ohmic and non-ohmic behavior. Also, anomalous values of the potential barrier are observed due to interface properties which make non-ohmic contacts behave as ohmic ones [2.4].

The space-charge limited conduction (SCLC) [2.5] and the well-known injection models such as thermionic emission and Fowler-Nordheim tunneling, have described experimental current-voltage (*I*-*V*) measurements in metal-organic-metal devices quite accurately in certain voltage ranges where these phenomena are dominant. The inclusion of a temperature and electric field-dependent mobility in the Mott-Gurney's law has been used to explain experimental results [2.6] and to determine material characteristic parameters in the Gaussian disorder model [2.7]. The Mott-Gurney's current-voltage relation, $I \propto V^2$, often appears in experimental data [2.8], and [2.9]. For example, Mott-Gurney's law was used in [2.9] to explain the experimental current density-voltage (*j* vs. *V*) measurements for a 3,4,9,10-perylenetetracarboxylic dianhydride (PTCDA) organic layer sandwiched between two metal electrodes.

However, this quadratic trend ($\boldsymbol{j} \propto \boldsymbol{V}^2$) is only valid for a certain current range. Outside this interval, different *j–V* relations appear and other models must be used.

In reference [2.3], the measured electrical data for single carrier hole-only diodes based on MEH-PPV (poly(2-methoxy,5-(2'-ethyl-hexoxy)-1,4-phenylene-vinylene)) exhibited a weak temperature-dependent current with this organic material. This behavior could not be explained by the thermionic emission model, and instead, a tunneling model was proposed. However, the tunneling injection does not support a variation with temperature and an expression that fits and predicts experimental *j–T* curves is not available.

Reduction/oxidation (REDOX) reactions are also incorporated in the transport mechanism [2.9], [2.10], [2.11], and a theoretical and quantitative redox-reaction model has been proposed [2.11]. This model is based on the fact that the charges on cations and anions that are transported along the device are formed at the interfaces by redox reactions.

The mechanisms cited above have one common feature: an external bias voltage is needed to support the physical and chemical processes in the organic diodes. However, a compact model that combines these physical aspects with the redox reaction, and provides an explanation of the *j-V* curves in the whole range of voltage biasing, is lacking. The objective of this work is to propose such a model.

This chapter is organized as follows. In section 2.2, we propose a model that combines all the key phenomena that occur inside organic diodes: phenomena such as carrier injection, ion formation and charge transport. A voltage expression depending on the current density *j* is deduced for each phenomenon and a method to obtain the global *j–V* and *j–T* curves is proposed and explained. A temperature-dependent mobility is also incorporated in the proposed model. Then, an equivalent circuit (see Fig. 2.1) of the

model is proposed. In Section 2.3, the behavior and predictions of the proposed model are presented and discussed. Different cases are studied, depending on whether the contacts are ohmic or rectifying. Then, a comparison of the results of our model to published experimental data is presented and discussed. The importance of considering all the mechanisms that take place during the charge transport in the organic material (redox reactions, tunneling and thermionic emission effects), and the key features of each one of these mechanisms, are highlighted in the interpretation of the experimental data.

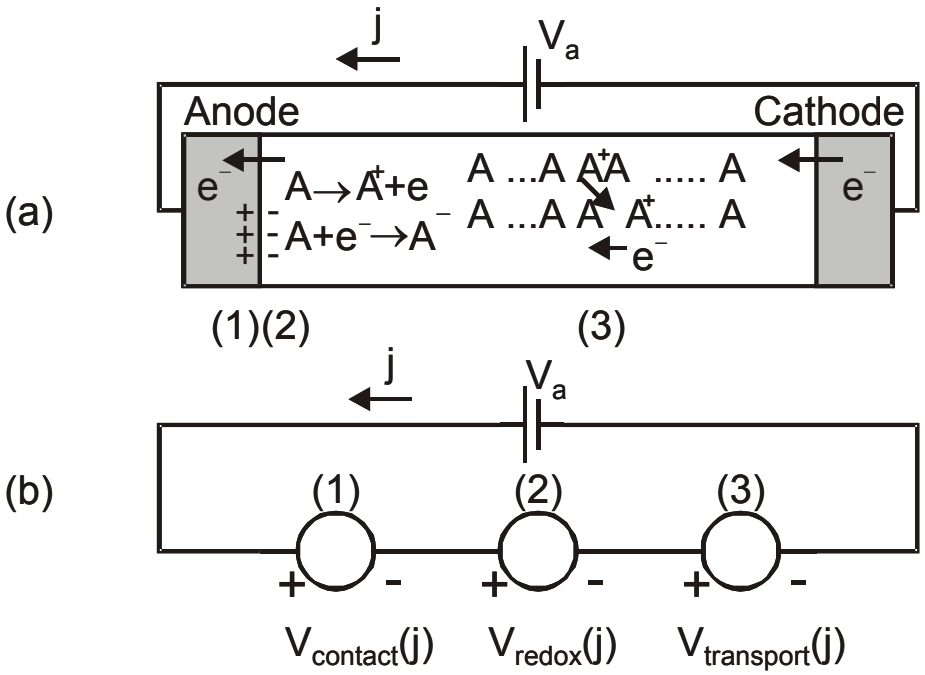

Figure 2.1. (a) Schematic diagram of an organic device. (1) Electrons from the organic layer pass the barrier at the anode interface; (2) this barrier is reduced by the formation of charges at the interface; (3) transfer of electrons between neutral molecules and oxidized ions takes place, resulting in a positive charge swept by the electric field towards the cathode. (b) Equivalent circuit of the organic diode. For a given current, the voltage components across the organic diode are (1) the contact voltage, (2) the potential needed to sustain a redox reaction, and (3) the voltage required for the transport of charge.

2.2 Mechanisms that Govern the Injection and Transport of Charge.

Our proposed model is based on a generic metal/organic/metal structure which is shown in Fig. 2.1a. The current-voltage characteristics can be understood by assuming that the following three phenomena take place within the organic material.

(1) Charge carriers must pass the barrier at the contacts.

(2) Ions are created at the electrodes by a redox reaction in the organic material. These ions form charged dipoles which modulate the injection barrier.

(3) Transport is then supported by the drift of the injected charges.

Thus, to maintain a current density j, the applied voltage, V_a, is shared by voltages required for ion formation, V_{redox}, for charge transport, $V_{transport}$, and for carrier injection through a barrier, $V_{contact}$. The relationship between the applied voltage V_a and the current density through the structure is described by the equivalent circuit of Fig. 2.1b, in which

$$V_a = V_{redox}(j) + V_{transport}(j) + V_{contact}(j). \tag{2.1}$$

In a typical 2-terminal organic device, the organic material is placed between a metallic anode and a metallic cathode, and a voltage V_a is applied as shown in Fig. 2.1a. The device length, L, is the distance from the anode to the cathode and is defined along the x-axis. For simplicity, only the displacement of positive charge is considered.

The energy diagrams of the constituents of a generic metal/organic/metal structure with different metals at the anode and cathode are shown in Fig. 2.2a where they are represented prior to contact and under the assumption of common vacuum level at each material surface [2.12]. The energy diagram of the structure in equilibrium after contact

is depicted in Fig. 2.2b. A barrier is seen from the metals towards the organic material. The height of the barrier (φ_M) is the difference between the metal Fermi level and the organic material's highest occupied molecular orbital (HOMO) level [2.13], [2.14], [2.15].

A tail distribution of negatively charged electrons from the metal [2.12], [2.16], [2.17], may fill the lowest unoccupied molecular orbital (LUMO) and higher organic levels, bending the energy levels at the organic-metal interface. The variables $V_{bMi}(0)$ (i=1,2) measure this bending at the metal-organic interface. The central regions of the organic layer, which are far from the interfaces, do not feel the influence of the metal and the volume of the organic material can be assumed neutral. The Fermi level or average electronic energy and the HOMO level are closer to each other in the volume than at the organic/metal interface.

In equilibrium, the sum of all these potential barriers φ_{Mi} and $V_{bMi}(0)$, (i=1,2) throughout the device must be zero, that is

$$\left[\varphi_{M1} - V_{bM1}(0)\right] - \left[\varphi_{M2} - V_{bM2}(0)\right] = 0 . \tag{2.2}$$

If an external voltage (V_a) is applied to the device (Fig. 2.2c), then a positive current from the anode to the cathode flows through the device. In this configuration, the contact between the anode and the organic material is reverse biased (rectifying contact) and the contact between the organic material and the cathode is forward biased (ohmic contact).

The current through the left contact is limited by the thermionic saturation current value, unless the applied voltage is high enough for tunneling injection to take place. No limit of the current is imposed on the right contact. With these assumptions, the predicted behavior of the device depends exclusively on the nature of the rectifying contact.

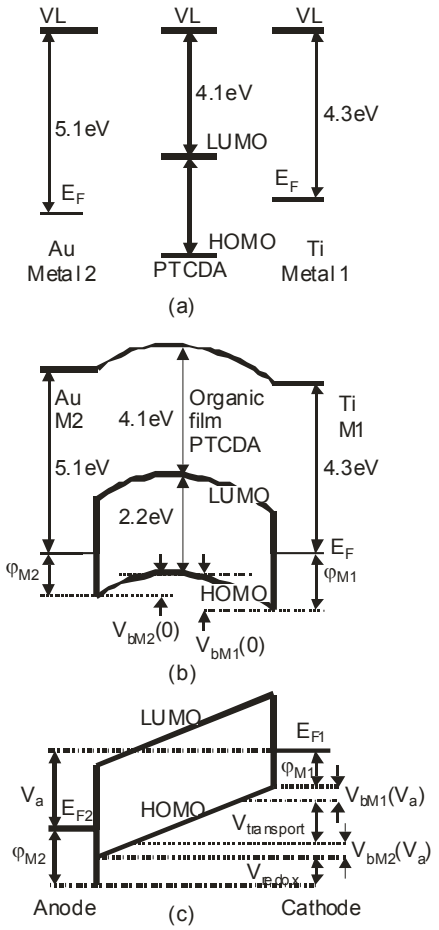

Figure 2.2. Schematic energy diagrams of a metal/organic/metal structure formed by two metals with different work functions. Gold–3,4,9,10-perylenetetracarboxylic dianhydride (PTCDA)–titanium is used in this figure. The Fermi level, E_F, the vacuum level, VL, the highest occupied molecular orbital (HOMO) and the lowest unoccupied molecular orbital (LUMO) are depicted. (a) Electronic structure of the three materials. (b) Energy diagram of the structure in equilibrium. A barrier, $\varphi_{M,}$ which is the difference between the metal Fermi level and the organic HOMO, prevents carriers from crossing to the organic layer. (c) Under the application of an external voltage, V_a, the energy levels of LUMO and HOMO are modified, as well as the barrier of the injecting contact due to the effect of charges at the interface. V_{redox} is the voltage needed to create the charges at the organic-metal interface. $V_{transport}$ is the voltage for charge carrier transport, and the difference $[\varphi_{M1,2}–V_{bM1,2}(V_a)]$ is the voltage drop at the contacts.

Having an external voltage, V_a, applied to the device, the HOMO and LUMO levels are modified (Fig. 2.2c). In addition, the barrier at the injecting contact changes due to the effect of the Nernst potential, V_{redox}, that is necessary to create the charges at the organic-metal interface [2.12], [2.13]. This effect of barrier reduction by the creation of charges at the interfaces may be similar to that reported in the literature, where polar

molecules are used to tune the work function of metals, thus making carrier injection from the electrodes into the organic material more favorable [2.2], [2.4].

Considering all the voltage drops in Fig. 2.2c, the applied voltage, V_a, given in (2.1) can be written as

$$V_a = \left[\varphi_{M1} - V_{bM1}(V_a)\right] + V_{transport} + V_{redox} - \left[\varphi_{M2} - V_{bM2}(V_a)\right], \tag{2.3}$$

where $[\varphi_{Mi} - V_{bMi}(V_a)]$, ($i$=1,2) is the voltage drop at the contact i for an applied voltage, V_a. The potential bending variables $V_{bMi}(V_a)$ (i=1,2) have positive values when the HOMO level at the metal-organic interface is lower than that in the bulk of the organic material. In Fig. 2.2c, $V_{bM1}(V_a)<0$ and $V_{bM2}(V_a)>0$.

Three cases can be studied depending on the height of the barrier φ_{Mi} *(i=1,2)*:

1) no injection, and thus no current,

2) thermionic emission through a barrier modulated by the voltage V_{redox}, and

3) tunnel injection through a barrier modulated by the voltage V_{redox}.

In the following subsections, the terms of equation (2.3) are calculated for these three cases.

2.2.1 - Redox and Charge Transport Equations

The voltage required for the redox process, V_{redox}, is calculated by using the Nernst equation, which is physically justified by means of the lattice-gas model [2.18], and whose value is given by:

$$V_{redox} = \Phi + V_t(T) \ln \frac{p^o}{\rho_m} \tag{2.4}$$

where p^o is the value of the ion density at the interface between the organic material and the metal, Φ is a constant which depends on the material involved in a given redox

reaction, ρ_m is the molecular density of the organic material, and $V_t(T) \equiv \frac{kT}{e}$ is the thermal voltage, where T is the absolute temperature, k is the Boltzmann's constant and e is the magnitude of the electron charge.

Organic materials do not possess intrinsic charges because their HOMO-LUMO gap values are significantly larger than the thermal energy. The charges that have been created at the surface of the electrode move through the organic material due to the electric field and the charge transport is space-charge limited. Only the free charge with density p_f contributes to a drift current density j, given by

$$j = e\mu p_f E\,, \tag{2.5}$$

where μ is the carrier mobility in the organic material and E is the electric field. If trapping mechanisms are considered inside the organic material, then the free charge density, p_f, will be related to the total charge density, p, by $p_f=\theta p$, where θ is the ratio of free to total charge density.

The electric field, according to Poisson´s equation, is

$$\frac{dE}{dx} = \frac{e}{\varepsilon}\frac{p_f}{\theta}\,, \tag{2.6}$$

where ε is the permittivity of the material.

Substituting (2.5) in (2.6), we get an expression for the current density j

$$j = \varepsilon\mu\theta E\frac{dE}{dx}\,, \tag{2.7}$$

which can be integrated from the organic material layer close to the anode ($x = 0^+$) to a given point x inside the material, resulting in

$$E(x)^2 = E(0)^2 + \frac{2j}{\varepsilon\mu\theta}x\,. \tag{2.8}$$

By assuming that the electric field is zero at the anode ($E(0) = 0$), then we can integrate (2.8) to obtain the transport voltage. The resulting relation is the well known Mott-Gurney's [2.5] or Child-Langmuir's law:

$$j = \frac{9}{8}\varepsilon\mu\theta\frac{V_{transport}^2}{L^3}. \tag{2.9}$$

The electric field according to the Mott-Gurney's law is:

$$E(x) = \left[\frac{2j}{\varepsilon\theta\mu}x\right]^{\frac{1}{2}}, \tag{2.10}$$

and the distribution of the free charge density, p_f, comes from the drift equation (2.5) and the electric field given in (2.10), so

$$p_f(x) = \left[\frac{j\varepsilon\theta}{2e^2\mu x}\right]^{\frac{1}{2}}. \tag{2.11}$$

This expression results in an infinite free charge density at the metal-organic interface. However, organic materials have a much lower carrier concentration than that of common semiconductor materials, making the assumption $E(0) = 0$ open to debate [2.11]. We have to note that this boundary still lies in the organic material and not in the metal.

In our model, we propose that the field at the boundary can be expressed in terms of a finite charge density $p(x = 0)$ and the value of this charge density equals the value of the ion density, p^o, given in the redox reaction (2.4): $p(x = 0) \equiv p^o$.

Equation (2.5) gives the electric field at the anode in terms of the current at steady-state:

$$E(0^+) = \frac{j}{e\mu\theta p^o}. \tag{2.12}$$

Substituting (2.12) in (2.8) gives

$$E(x) = \left\{ \frac{2j}{\varepsilon\mu\theta} \left[\frac{j\varepsilon\theta}{2e^2\mu\left(\theta p^o\right)^2} + x \right] \right\}^{\frac{1}{2}} \equiv \left\{ \frac{2j}{\varepsilon\mu\theta} \left[x_c + x \right] \right\}^{\frac{1}{2}}, \tag{2.13}$$

where we have defined a characteristic length, x_c, over which the charge density decreases to $1/\sqrt{2}$ of its initial value [2.11], given by

$$x_c(j, p^o) = \frac{j\varepsilon\theta}{2e^2\mu(\theta p^o)^2}. \tag{2.14}$$

Integrating (2.13), we obtain the transport voltage, $V_{transport}$, required to move the charge across the organic material:

$$V_{transport} \equiv \Delta V = \frac{2}{3} \left\{ \frac{2j}{\varepsilon\mu\theta} \right\}^{\frac{1}{2}} \left[\left[x_c(j, p^o) + L \right]^{\frac{3}{2}} - \left[x_c(j, p^o) \right]^{\frac{3}{2}} \right]. \tag{2.15}$$

The model is also valid for cases in which the mobility is not constant. In these cases, a thermally-activated mobility behavior observed in [2.6], [2.19], [2.20] can be introduced in the previous expressions. The mobility for those cases is given by

$$\mu = \mu_o \exp\left(-\frac{\Delta}{k_B T} \right), \tag{2.16}$$

where μ_o is the mobility prefactor and Δ is the activation energy.

Once the expressions for V_{redox} and $V_{transport}$ in (2.1) are obtained by (2.4) and (2.15) respectively, our next step is to discuss the expression that is needed to calculate the voltage, $V_{contact}$, required for the carrier injection through the contact barrier. With this aim and for a straightforward reading, the well-known expressions for tunneling and thermionic injection phenomena will be briefly described in the next subsections.

2.2.2 - Injection Models

In general, injection through a barrier is the combination of both thermionic and tunneling phenomena. In the case of low electric fields, tunneling injection is negligible and thermionic emission dominates. The thermionic emission theory assumes that carriers, with energy larger than the top of the barrier, will cross the barrier when they move towards the barrier. The actual shape of the barrier is hereby ignored. At a given temperature, T, the thermionic emission current density for a barrier height, φ_M, and applied voltage, V_a, can be expressed as

$$j = A^* T^2 e^{-\frac{\varphi_M}{V_t}} (1 - e^{\frac{-V_a}{nV_t}}) \equiv j_{os}(T)(1 - e^{\frac{-V_a}{nV_t}}), \qquad (2.17)$$

where $A^* = \frac{4\pi e m^* k^2}{h^3}$ is the Richardson´s constant, m^* is the effective mass of the carriers, h is Planck's constant and n is the diode´s ideality factor. The sign of j in (2.17) is defined positive from the anode to the organic layer (Fig. 2.1a), and V_a is the applied voltage between the anode and cathode.

In the case of high barriers, thermionic emission is negligible and tunneling is the main injection mechanism. High electric fields are needed to get measurable values of the current density. For a barrier height, φ_M, and an applied electric field E, the Fowler-Nordheim tunneling injection current density j [2.21] is:

$$j \propto E^2 \exp\left(-\frac{\kappa}{E}\right), \qquad (2.18)$$

where κ is a parameter that depends on the barrier shape. Assuming that the electric field is constant along the polymer, then the shape of the barrier can be considered to be triangular, and κ [2.21] is:

$$\kappa = \frac{8\pi\sqrt{2m^*}\varphi_M^{\frac{3}{2}}}{3qh}. \tag{2.19}$$

2.2.3 - Transport Equations in Organic Diodes - Thermionic Emission

In this subsection, the equations for the redox, transport and thermionic mechanisms are combined. Also, the method to build the current-voltage curves for different contact barrier heights is described.

Assuming a structure like that represented in Fig. 2.2c with V_a >0, carriers at the injecting contact find a barrier, φ_{M2}. Typical values of the difference between the metal work function and organic HOMO produce a large barrier height, φ_M, (see Tables 2.1 and 2.2). This barrier prevented the flow of charge through the contact and only a saturation current density would appear. However, many experiments show the usual j–V curve of a forward biased diode [2.2], [2.4], [2.8], [2.9], [2.10], [2.14]. A barrier reduction is a plausible way to interpret experimental data. In fact, polar molecules are intentionally introduced near the interfaces to alter the work function of metals [2]. After a careful study of these results, we propose the barrier reduction by the creation of charges near the interfaces by the redox reaction.

The injecting contact barrier is reduced from its initial value φ_M to (φ_M–V_{redox}) and the modified injected current density is

$$j = A^* T^2 e^{-\left(\frac{\varphi_M - V_{redox}}{V_t}\right)}\left(1 - e^{\frac{-V_a}{nV_t}}\right), \tag{2.20}$$

where V_a is given in equation (2.1).

Table 2.1. Energy levels of the organic semiconductors referred to in this chapter.

Organic or polymer film	HOMO (eV)	LUMO (eV)	HOMO-LUMO gap (eV)	Reference, Year
PTCDA	6.3–6.8	4.1–4.6	2.1	[2.4], 1996 [2.13], 2000
MEH-PPV	4.9–5.6	2.8–3.8	–	[2.2], 2005 [2.3], 1994 [2.25], 2005
PPV	5	2.5	–	[2.14], 2005
PEDOT	5.02	3.42	1.6	[2.14], 2005
Alq3	5.6–5.8	2.5–3.2	2.9	[2.26], 1998 [2.27], 2006
TPD	5.1–5.44	1.8–2.1	3.4	[2.26], 1998
alfa-NPD	5.4	2.3	3.1	[2.13], 2000
pentacene	4.8–5.0	2.5	–	[2.28], 2007
NPB	5.2	2.1	3.1	[2.29], 1999

Assuming that the main contributions to band bending lie in the terms V_{redox}, and $V_{transport}$, we can consider that

$$\left[\varphi_{M1} - V_{bM1}(V_a)\right] - \left[\varphi_{M2} - V_{bM2}(V_a)\right] \approx \left[\varphi_{M1} - V_{bM1}(0)\right] - \left[\varphi_{M2} - V_{bM2}(0)\right] = 0, \qquad (2.21)$$

which together with (2.3) results in

$$V_a \approx V_{redox}(j) + V_{transport}(j). \qquad (2.22)$$

Thus, the applied voltage, V_a, required to maintain a current density, j, is shared by charge formation at the metal–organic interface, V_{redox}, and in SCLC transport, $V_{transport}$. Therefore, (2.20) can be rewritten as

$$j = A^* T^2 e^{-\frac{\varphi_M}{V_t}} e^{\frac{V_{redox}}{V_t}} \left[1 - e^{-\left(\frac{V_{redox}+V_{transport}}{nV_t} \right)} \right] = j_{os}(T) e^{\frac{V_{redox}}{V_t}} \left[1 - e^{-\left(\frac{V_{redox}+V_{transport}}{nV_t} \right)} \right], \tag{2.23}$$

and the saturation current j_{os}(T), becomes modulated by the redox potential.

For a given current density j, (2.23) provides a relation between the redox voltage and the transport voltage j=f(V_{redox}, $V_{transport}$). Combining (2.14) and (2.15), a relation between $V_{transport}$, the current density j and the total ion density p^o, created by the redox reaction at the interface is obtained,

$$V_{transport} = \frac{2}{3} \left(\frac{2j}{\varepsilon \mu \theta} \right)^{\frac{1}{2}} \left\{ \left[L + \frac{j\varepsilon}{2e^2 \mu \left[p^o \right]^2} \right]^{\frac{3}{2}} - \left[\frac{j\varepsilon}{2e^2 \mu \left[p^o \right]^2} \right]^{\frac{3}{2}} \right\}. \tag{2.24}$$

From (2.4), we obtain p^o as a function of V_{redox}. Including this relation in (2.24), we get

$$V_{transport} = \frac{2}{3} \left(\frac{2j}{\varepsilon \mu \theta} \right)^{\frac{1}{2}} \left\{ \left[L + \frac{j\varepsilon}{2e^2 \mu \left[\rho_m e^{\frac{V_{redox}-\Phi}{v_t(T)}} \right]^2} \right]^{\frac{3}{2}} - \left[\frac{j\varepsilon}{2e^2 \mu \left[\rho_m e^{\frac{V_{redox}-\Phi}{v_t(T)}} \right]^2} \right]^{\frac{3}{2}} \right\}. \tag{2.25}$$

Equation (2.25) gives us an extra relation between V_{redox} and $V_{transport}$, which together with (2.23), allow us to calculate the current density as a function of the applied voltage. This method also provides a way to determine the distribution of charge density along the organic layer. According to the Poisson equation, the charge density is proportional to the derivative of the electric field. When we differentiate the electric field obtained in our model (2.13), we obtain the distribution of the charge density along the organic layer:

$$p(x,j) = \frac{p^o(j)}{\sqrt{1+\frac{x}{x_c(j)}}}. \tag{2.26}$$

Table 2.2. Electrode work functions of the metals and metal/(Self assembled monolayer) referred to in this chapter.

Electrode	Work function (eV)	Reference, Year
Indium	4.12	[2.4], 1996
Tin	4.42	[2.4], 1996
Titanium	4.33	[2.4], 1996
Aluminum	4.25–4.33	[2.4], 1996
Silver	4.26–4.74	[2.2], 2005 [2.4], 1996
Ag_$HSC_2H_4C_6F_{17}$	5.5	[2.2], 2005
Gold	4.9–5.47	[2.2], 2005 [2.4], 1996
Calcium	2.9	[2.3], 1994
Indium tin oxide	4.3−4.7	[2.3], 1994 [2.25], 2005
Magnesium	3.7	[2.13], 2000

In order to obtain a *j-T* curve for an applied voltage V_a, a numerical procedure is followed. The current density j_c for a given temperature T_c is obtained from the set of equations (2.22), (2.23), (2.14), (2.15), and (2.16). At given voltage across the diode V_a, (2.22), (2.23) and (2.25) provide relations between V_{redox}, $V_{transport}$ and j_c. The temperature dependence is included in (2.25) via the mobility from (2.16). A numerical

procedure was used to obtain the desired voltage V_a across the diode by changing the current density j_c at given temperature T_c.

2.2.4 - Transport Equations in Organic Diodes - Tunneling Injection

Another case of interest is a material in which the barrier reduction by redox reactions is not enough to obtain a non-zero current by thermionic injection. In this case, injection is only plausible at high electric fields by the tunneling effect.

The assumptions that the contributions to band bending lie in the terms V_{redox}, and $V_{transport}$ that were made in subsection 2.2.3 to get j–V curves need to be modified accordingly. The main differences from the previous case are:

1. The anode barrier is much higher than the effect of barrier reduction by creation of charge. Thus, the following simplification can be used

$$\varphi_{M2} - V_{redox} \approx \varphi_{M2}; \tag{2.27}$$

2. The voltage drop at the anode is much higher than the drop at the cathode, that is

$$[\varphi_{M2} - V_{bM2}] >> [\varphi_{M1} - V_{bM1}]. \tag{2.28}$$

Under these assumptions, (2.3) reduces to:

$$V_a \approx V_{transport} + [V_{bM2}(V_a) - \varphi_{M2}] \equiv V_{transport} + V_{c2}, \tag{2.29}$$

where the voltage drop at the charge injecting contact is denoted by V_{c2}.

In order to find a relation between the current density and the applied voltage V_a, we examine (2.18). Next, we should establish a relation between the electric field E and the applied voltage V_a. The most common assumption is a constant electric field

throughout the whole organic material. Assuming only a region of constant high electric field means that either tunnel or SCLC transport is dominant. Experimental data in metal-organic-metal structures can be reproduced with existing tunnel expressions [2.3]. However, considering tunneling as the only mechanism that is present in the organic material may not be a valid approximation, unless this material has a high conductivity. Our model considers that the sample of length L, is divided into two parts. The first part is one of length $x_t<L$, where tunneling takes place and the electric field is assumed constant with a value:

$$E = -\frac{V_{c2}}{x_t} \tag{2.30}$$

and the potential varies linearly as $V(x) = \frac{V_{c2}}{x_t} x$. The second region of length $L-x_t$ is dominated by the SCLC model [2.5]. The transport term is determined by integration of the electric field in this region and $V_{transport}$ is given by:

$$V_{transport} = V(L) - V(x_t) = \frac{2}{3}\left\{\frac{2j}{\varepsilon\mu\theta}\right\}^{\frac{1}{2}}\left[\left[x_c + (L-x_t)\right]^{\frac{3}{2}} - x_c^{\frac{3}{2}}\right]. \tag{2.31}$$

For low current densities and high charge density, p^o, (2.14) gives a low value for the characteristic length, x_c, and $V_{transport}$ can be approximated as:

$$V_{transport} \approx \frac{2}{3}\left\{\frac{2j(L-x_t)^3}{\varepsilon\mu\theta}\right\}^{\frac{1}{2}}. \tag{2.32}$$

The substitution of (2.30) into (2.18) gives us the anode voltage drop, V_{c2} for a given current density j; equation (2.32) allows us to calculate the transport voltage, $V_{transport}$; finally a point (j, V_a) is obtained using (2.29). Repeating this procedure for different current densities, we obtain the current-voltage curve.

As in the previous subsection, our model is sensitive to temperature variations. A thermally activated mobility can incorporate such a dependence. Tunnel injection by itself does not support temperature variations (see (2.18)). However, non-negligible variations of the current with the temperature have been observed in experimental measurements taken in samples that are supposed to undergo tunnel injection [2.3]. In order to interpret such experiments, we also propose a method to obtain a *j*-*T* curve at an applied voltage V_a.

Given a temperature T, we choose a current density value j and then calculate its associated applied voltage V_a as described below. For the current density j, the contact voltage drop, V_{c2}, is calculated by using the Fowler-Nordheim (2.18) together with the parameter x_t from (2.30). The transport voltage ($V_{transport}$) is obtained by using (2.29): $V_{transport} \approx V_a - V_{c2}$. Equation (2.32) together with the thermally activated mobility, (2.16), confirms the temperature T associated with the current density j. Repeating this procedure for several values of current densities, we obtain the desired *j*-*T* curve.

2.2.5 - Organic Diode Equivalent Circuit

The relationship between the applied voltage, V_a, and the current density, j, is described by the equivalent circuit of Fig. 2.1b. However, two cases have been distinguished above depending on the value of the barrier height which defines the turn-on voltage of the device. When barrier height reduction by redox reactions makes thermionic injection favorable, the applied voltage depends on transport requirements and charge formation. In this case, the model of Fig. 2.1b is reduced to the model presented in Fig. 2.3a. The turn-on voltage is of the order of a few volts.

If the turn-on voltage is greater than a few volts, then the barrier reduction due to charge formation can be neglected and the applied voltage depends on the voltage across the contact, $V_{contact}$, and on the transport requirements, $V_{transport}$. For this case, the

simplified model is presented in Fig. 2.3b.

Our model allows for the incorporation of other phenomena such as leakage current effects. It has been reported that organic films interact with ambient atmosphere [2.1], even hydrophobic pentacene can absorb water or oxygen molecules from the air [2.22]. This interaction results in an off-current increase which may not be negligible. A current source can be added in parallel to the other elements, Fig. 2.3c, to model this effect

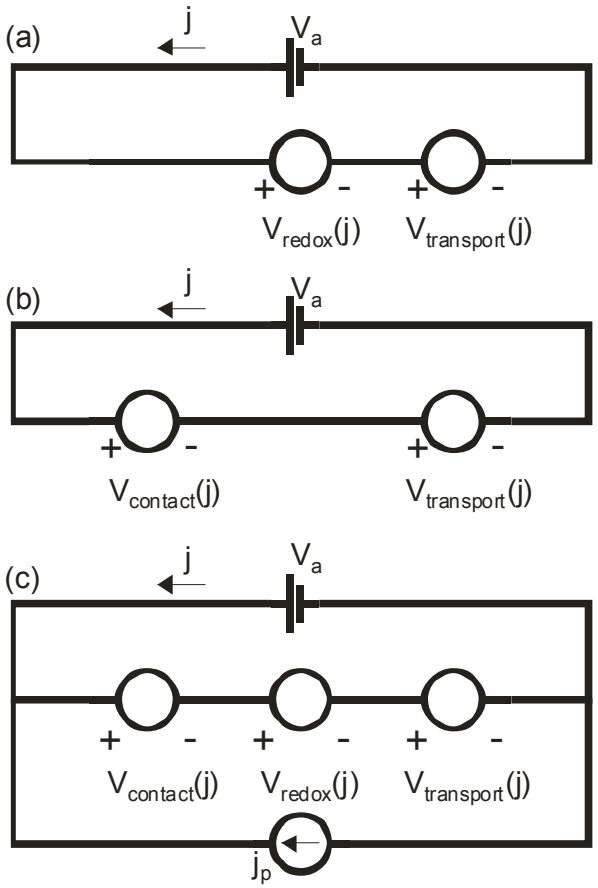

Figure 2.3. (a) Equivalent circuit for organic diodes with turn-on voltage of few volts. The applied voltage is employed in transport requirements and charge creation at the anode-organic interface. (b) Equivalent circuit for organic diodes with high turn-on voltage (around ten volts). The applied voltage is employed in transport requirements and the voltage needed to surpass the barrier. (c) Complete equivalent circuit of an organic diode including leakage currents, j_p.

2.3 Voltage and Temperature Dependence of the Current

In this section, typical *j-V* and *j-T* curves for the cases presented in the previous section are discussed. In these curves, the importance of the mechanisms detailed in this chapter (redox potential, space charge transport model, thermionic emission and tunneling through a barrier) is shown. The limits in which any mechanism is dominant over the rest are studied. The different *j–V* and *j–T* behaviors predicted by our model explain experimental data from the literature. In this study, we use characteristic values of materials taken from literature. The values for the energy levels of the organic semiconductors and the electrode work functions are summarized in Tables 2.1 and 2.2. The value of the relative permittivity for organic materials is considered to be around 3, (ε~3), as reported in [2.1], [2.9], [2.15]. Finally, the values for the mobility in organic materials are taken in the interval [10^{-6}, 5×10^{-4}] $cm^2V^{-1}s^{-1}$, [2.1].

2.3.1 - Thermionic Emission Case

2.3.1.1 *j-V* Curves

In this case, the redox voltage modulates the injection barrier as was described in Section 2.2.3. In order to get a positive current density through the barrier, values of the redox voltage lower than the value of the material's natural barrier are needed. The redox voltage is close to zero for low current densities and increases in value for higher currents, but this voltage is always within a narrow range of values.

This is shown in Fig. 2.4 where the redox potential, V_{redox}, (dotted line) is represented for current densities within the interval [10^{-7}, 10^{0}] $A\cdot cm^{-2}$ for a silver/N,N'-diphenyl-N,N'-bis(3-methylphenyl)-[1,1'-biphenyl]-4,4'-diamine/Aluminum, Ag/TPD/Al organic diode.

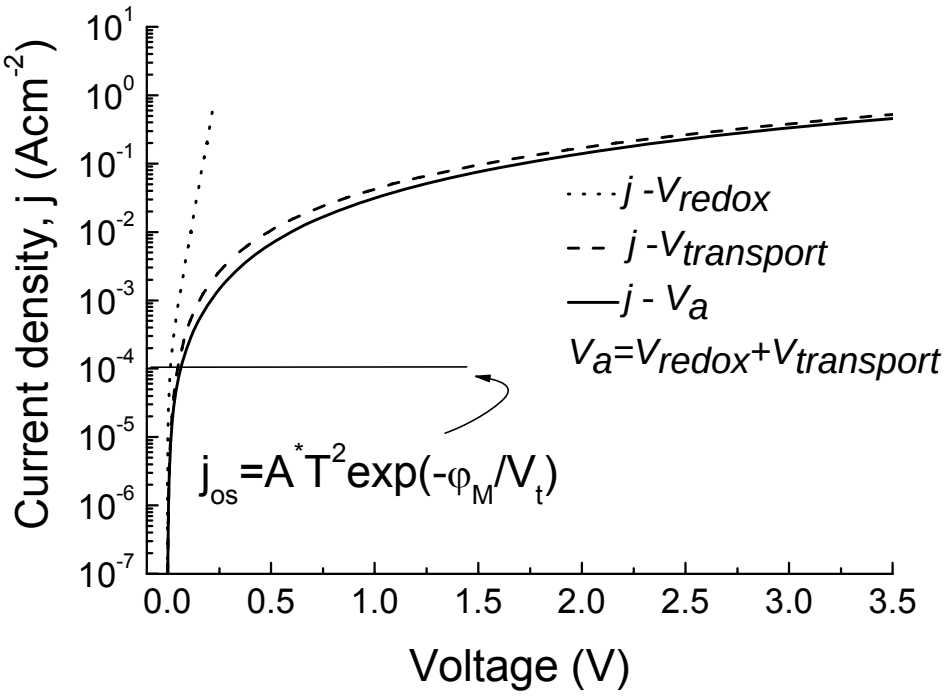

Figure 2.4. Current density as a function of the applied voltage, V_a for a Ag/TPD/Al organic diode (solid line); calculated current density as a function of the redox potential (dotted line); calculated current density as a function of the transport voltage (dashed line). Current densities are in the range 10^{-7} to 10^{0} A·cm^{-2}. The sample parameters are: L=150nm, ε=3.0, ρ_m=2×10^{21}cm^{-3}, μ=5×10^{-4}cm^{2}V^{-1}s^{-1}, φ_M= 0.65eV, Φ=0.36V. The horizontal solid line represents the value of the saturation current density.

The transport voltage, $V_{transport}$, (dashed line) and the sum of both contributions, V_{redox}+$V_{transport}$, (solid line) are also depicted in Fig. 2.4. The horizontal solid line represents the value of the saturation current, j_{os}. Our model allows currents greater than this value as j_{os} is modulated by the redox potential (see (2.23)).

In Fig. 2.5, a comparison between a *j-V* curve calculated by our model (solid line)

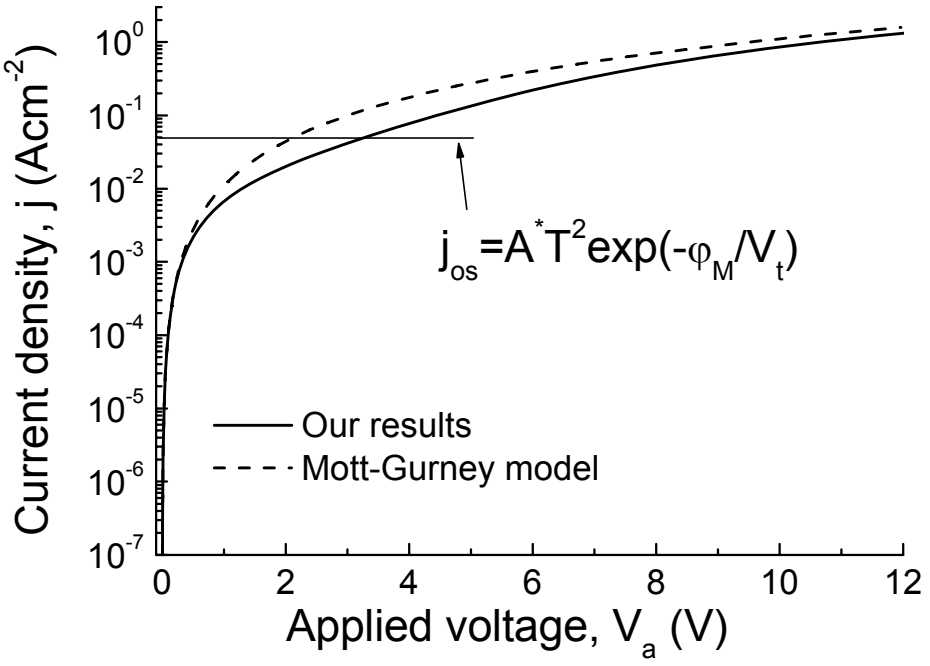

Figure 2.5. Calculated current density, *j*, as a function of the applied voltage for an ITO/4,4-bis-1-naphtyl-N-phenylaminobiphenyl (NPB)/Al organic diode. Comparison between our results (solid line) and the Mott-Gurney's law (Eq. (9)) (dashed line). The sample length is 150nm and the material parameters are: ε=3.5, ρ_m=2×10^{21}cm^{-3}, Φ=0.35V, μ=10^{-4} cm^2 V^{-1}s^{-1}, φ_M=0.5eV. Both models match at high and low currents, however, at current densities close to the thermionic saturation current (horizontal solid line) a difference appears.

and the *j–V* curve obtained by using the Mott-Gurney's relation (equation (2.9)-dashed line) is presented. The difference between the curves is negligible at both high and low currents, however, it is non-negligible at values of the current density close to the thermionic saturation current (horizontal solid line in Fig. 2.5), where our model predicts lower current density values. The explanation of the good agreement at low and high regimes is given below.

For low current densities, both transport, $V_{transport}$, and redox, V_{redox}, voltages are expected to be small. Under this assumption, (2.20) can be approximated as:

$$j \approx A^* T^2 \frac{V_{redox} + V_{transport}}{V_t} e^{-\frac{\varphi_M}{V_t}}. \tag{2.33}$$

We further assume that the transport term is negligible in comparison to the redox term (as justified above). Then

$$j \approx A^* T^2 e^{-\frac{\varphi_M}{V_t}} \frac{V_{redox}}{V_t}. \tag{2.34}$$

Including this approximation in (2.4), the characteristic length, x_c, given by (2.14), tends to zero as current density j decreases. This means that for low current densities, the transport term calculated by our model (2.15) tends to the Mott-Gurney's law [2.5] given by (2.9).

For high current densities and applied voltages, equation (2.20) can be approximated as

$$j \approx A^* T^2 e^{\frac{\varphi_M - V_{redox}}{V_t}}. \tag{2.35}$$

Including this approximation in (2.4), the characteristic length x_c (2.14) tends to zero as the current density j increases. As in the previous case, our transport term (2.15) converges to the Mott-Gurney's law (2.9).

In spite of this agreement at low and high voltages, our model has the following important advantages:

1. It takes into account characteristic parameters of the contact between the metal and the organic material (such as the barrier height).

2. It allows the evaluation of the charge density at the anode/organic interface.

3. The lower slope shown in Fig. 2.5 at intermediate currents allows a better interpretation of experimental data, as will be shown below.

A comparison between the experimental data reported in [2.23], the Mott-Gurney's prediction (dashed line) from (2.9) and our results (solid line) from (2.15) is depicted in Fig. 2.6a. A good agreement is shown between our results and the experimental data for Ag/aluminum tris(8-hydroxyquinoline) (Alq^3)/Ag and gold/4,4-bis-1-naphtyl-N-phenylaminobiphenyl(NPB)/gold organic diodes.

The two sets of curves in Fig. 2.6a correspond to two different states for the metal/organic/metal structures studied in [2.23]. For a given voltage, two different values of the current are possible, depending on the state of the traps in the device. When the traps are filled (off state), the system is blocked and the current density, $j_{off\ state}$, is lower than the current density, $j_{on\ state}$, when the traps are empty (on state). This phenomenon can be used to design memory devices.

To calculate the ratio of trapped charge, first, we calculate the curve which corresponds to the on-state by considering that all the created charge is free (that is, the parameter θ defined in Section 2.2, equals 1). Second, the ratio of free to total charge density is calculated by the fitting of the off-state experimental data, resulting in a value of θ=0.02. Only 2 percent of the created charge is mobile in the off state, values in the same range and even lower have been reported [2.24].

The inset of Fig. 2.6a) compares our model prediction for the on state and Mott-Gurney's law to experimental data in a linear scale. To obtain a good agreement with the experimental data, our model considers a finite charge density at the interface in the range $[4.3\times10^{-4}, 5.6\times10^{-4}]$ C·cm^{-3} for current densities within the interval $[10^{-7}, 10^{0}]$ Acm^{-2}. The large difference between the experimental data and the Mott-Gurney's law is because the finite charge density at the interface is neglected in Mott-Gurney's law, by assuming zero electric field at the anode contact. Our model considers the barrier at the metal anode contact while the barrier height is zero in Mott-Gurney's law.

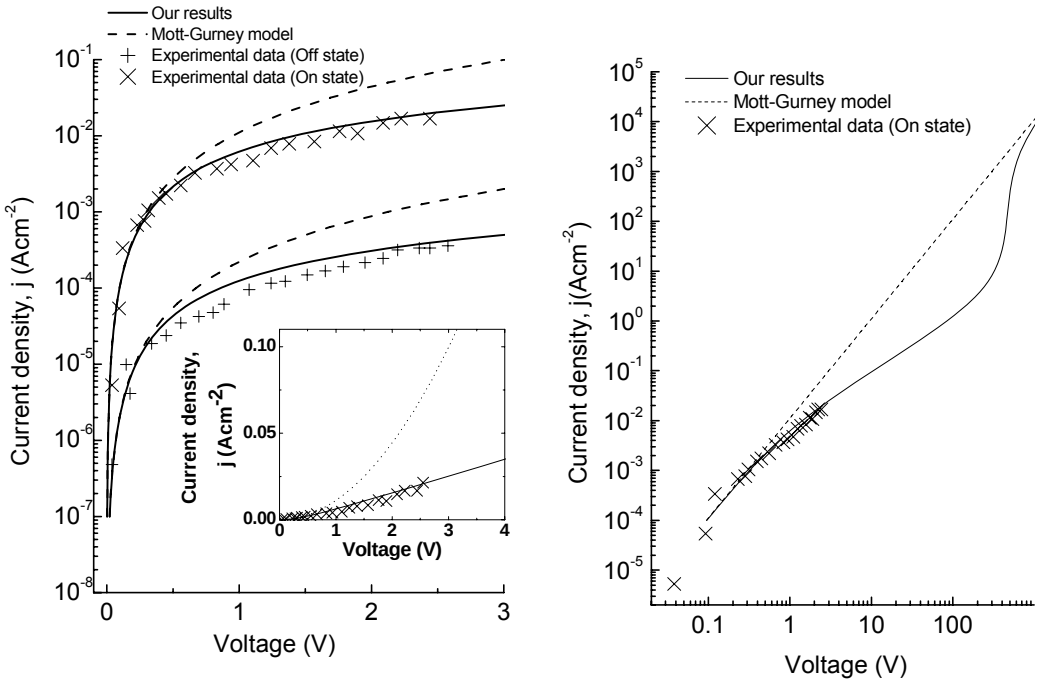

Figure 2.6. (a) Comparison of our experimental results (solid line) and experimental data measured in [2.23] (symbols) for gold/NPB/gold organic diode. The results predicted by the Mott-Gurney's law are represented in dashed line. The two sets of curves depicted in the figure represent two different states (on and off states, top and bottom curves, respectively), that are governed by trapped charge inside the organic film. The sample parameters are: L=150nm, ε=3.5, $\rho_m=2\times10^{21}\text{cm}^{-3}$, $\mu=10^{-4}\text{cm}^2\text{V}^{-1}\text{s}^{-1}$, φ_M= 0.4eV, Φ=0.35V. The trapping parameter for the off-state is θ=0.02, and θ=1.0 for the on-state. Inset: Comparison of our results, experimental data and Mott-Gurney's law in a linear scale, showing that our model explains the trend in the experimental data better. (b) Overlapping of our model and Mott-Gurney's law at high and low currents. The overlap at high currents is in a range, which is not accessible by experiments.

2.3.1.2 *j-T* Curves

As explained above, at low current densities, the global response of the device is limited by redox reactions (dotted line in Fig. 2.4). In this regime, the j–V response follows the thermionic emission expression (2.23) and current is expected to be strongly dependent on temperature. We can see this in Fig. 2.7, where current-voltage curves (Fig. 2.7a) and current-temperature curves (Fig. 2.7b and 2.7c) are represented for a Ti/PTCDA/Au organic diode. Fig. 2.7b depicts the calculated curve for the low injection regime, showing a strong temperature dependence. Within the high current

density regime, the *j–V* curve is determined by the transport term (dashed line in Fig. 2.4) and the thermal behavior is related to a temperature dependent mobility. Fig. 2.7c shows a weaker temperature dependence in this regime.

2.3.2 - Tunneling Injection Case

2.3.2.1 *j-V* Curves

The second case that we analyze is a rectifying contact with a high barrier φ_M. In this case, the thermionic injection current is negligible, the main injection mechanism is tunneling and the equivalent circuit is shown in Fig. 2.3b. A high applied electric field, *E,* is needed for measurable current densities. The electric field at the contact, *E,* is

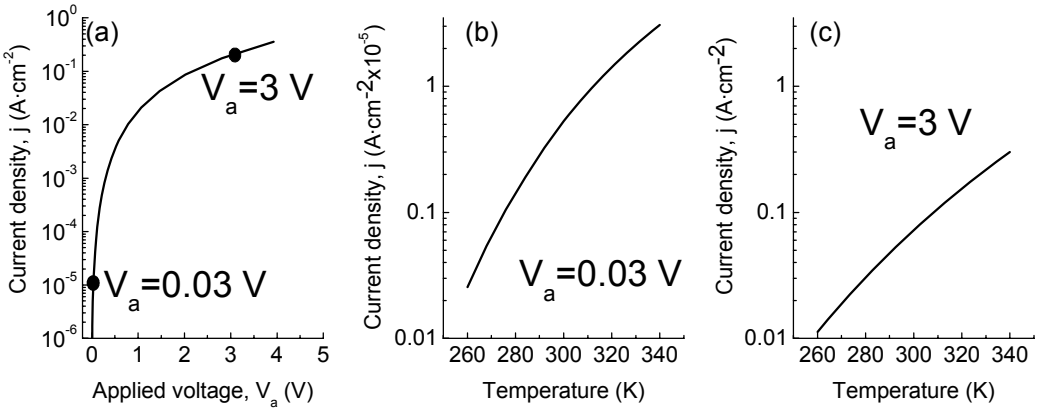

Figure 2.7. Calculated current density curves for a Ti/PTCDA/Au organic diode, (a) as a function of the applied voltage, V_a; and as a function of temperature for two applied voltages: (b) V_a = 0.03V, and (c) V_a = 3V. The current is strongly temperature dependent when V_a = 0.03V and the device response is controlled by thermionic emission. The current is less sensitive to temperature variations between 260K and 340K when V_a = 3V and the device response is controlled by transport requirements. The parameters of the sample used in these calculations are: L=150nm, ε=3.0, ρ_m=2×10^{21}cm^{-3}, mobility prefactor μ_o=16.8 cm^{2}V^{-1}s^{-1}, mobility activation energy Δ=0.3 eV (at room temperature the mobility is 10^{-4}cm^{2}V^{-1}s^{-1} according to (16)), a barrier height φ_M= 0.7eV, and a redox potential Φ=0.35V.

given by (2.30) and is high for large contact voltage drops, V_{c2}, and small tunneling distances, x_t.

The *j–V* curves predicted by our model are shown in Fig. 2.8. The parameters used

in this calculation are used later to explain experimental data and so the explanation of the values is given there. The solid line represents the global j–V curve, the transport component is represented by a dotted line and the tunnel component is depicted by a dashed line. Here, we can see that the limiting factor in the current through the device is tunnel injection. For example at a given current density of j=10^{-3} A·cm^{-2}, around ten volts is needed for tunnel injection, while a much smaller voltage, less than one volt, is required for charge transport through the organic material.

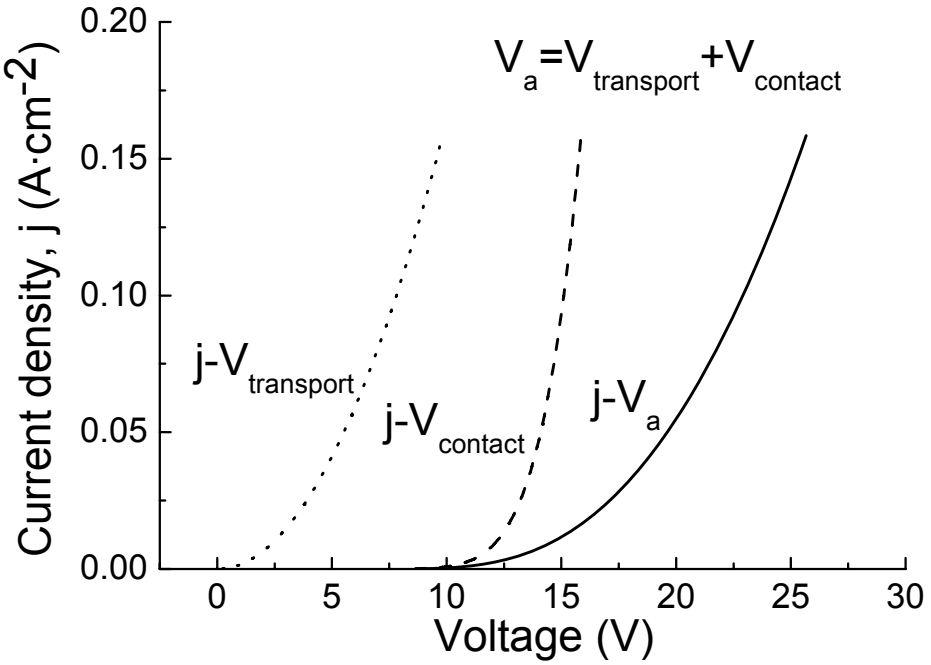

Figure 2.8. Representation of the current density, j, as a function of the applied voltage V_a and its components, tunneling ($V_{contact}$) and transport ($V_{transport}$). The sample parameters are: L=120nm, ε=3.0, ρ_m =2×10^{21} cm^{-3}, μ=4.0×10^{-6} cm^2 V^{-1}s^{-1}, φ_M =0.63eV and the electric field is: E=$V_{contact}$/(L/3.5).

According to our model, the global j–V response is determined by choosing a value of the current density j, then the voltage terms appearing in the model are calculated, and finally the total voltage is the sum of the voltage terms.

The tunnel injection component is clearly dominant in Fig. 2.8. However, the

transport term introduces a more physical explanation of experimental j–V curves. This fact can be seen in experimental measurement taken in [2.3]. There [2.3], the characteristics of single carrier hole-only diodes using MEH-PPV were studied, and measured j–V and j–T curves for the same device were presented.

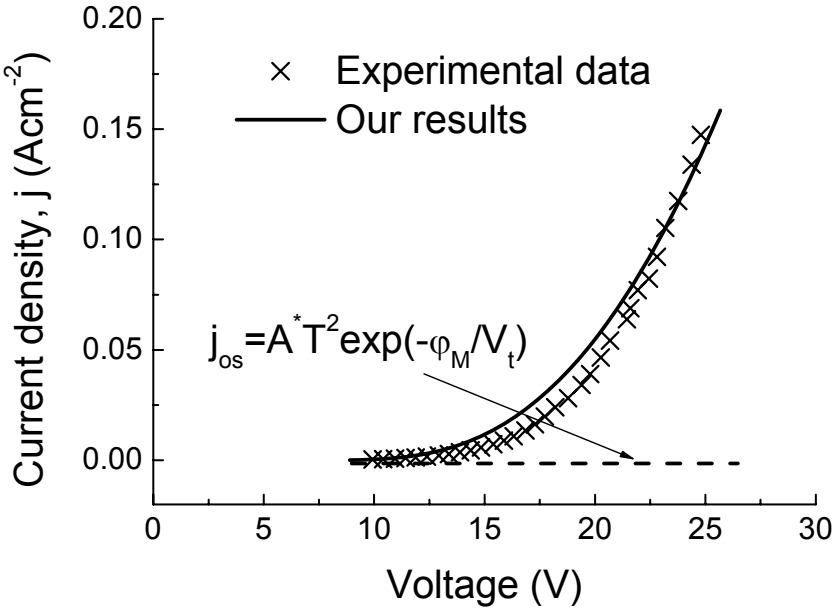

Figure 2.9. Comparison of the calculated current density as a function of the applied voltage (solid line) with experimental data taken from [2.3] (symbols) for a sample with the following parameters: L=120nm, ε = 3.0, ρ_m=2×10^{21}cm^{-3}, μ=4×10^{-6}cm^{2}V^{-1}s^{-1}, φ_M = 0.63eV, and a uniform electric field $E=V_{contact}/(L/3.5)$. The horizontal solid line represents the calculated thermionic saturation current for a barrier height of value φ_M = 0.63eV. Lower height barriers would produce a non negligible value for the thermionic saturation current.

Fig. 2.9 shows the comparison of a j–V experimental curve for a ITO/MEH-PPV/Au device (symbols) [2.3] with our numerical results (solid line). For a low barrier height, the current density due to thermionic emission is high according to (2.17) [2.9]. The maximum current that would support the thermionic emission model in this operation mode is the thermionic saturation current (horizontal line in Fig. 2.9). Its value is below the experimental data for a contact barrier of 0.63eV and would be higher than the experimental data for a lower contact barrier height. A barrier height of 0.63eV for the contact between ITO and MEH-PPV is a value within the range measured for these materials (see Tables 2.1 and 2.2).

The experimental $j-V$ curve could also be reproduced by the tunnel injection model alone [2.3]. However, reproducing these experimental data by the tunnel injection model alone means that the thermionic emission is negligible. Moreover, neglecting the transport term means that x_t (see (2.30)) occupies the whole organic film ($x_t = L$). The electric field necessary to support a current j is then lower and the barrier height should decrease accordingly. However, this decrease would have some problems as thermionic emission might take place, which contradicts the assumption of a negligible thermionic current. Our model solves this problem by the division of the sample in two regions, one for the charge transport and the other for the tunneling injection (see Section 2.2.4). For a barrier height of 0.63eV, a tunneling distance $x_t = L/3.5$ results in the electric field which explains the experimental data.

2.3.2.2 Temperature Dependence

Another important observation from Fig. 2.8 is that the transport term, although smaller than the contact voltage, defines the slope of the $j-V$ curve, in particular at high currents. This contribution is of special interest, since it allows the incorporation of a temperature-dependent term in the current density.

For low current densities, the applied voltage lies almost completely in the voltage that carriers need to surpass the contact barrier: the $j-V$ response follows the Fowler-Nordheim expression, and the current is expected to be independent of temperature.

To show these differences at low and high injection regimes, we have calculated a $j-V$ curve (Fig. 2.10a) for an ITO/MEH-PPV/Au organic diode sample. At two different values of the applied voltage, V_a=24V (high current regime) and V_a=9V (low current regime), the dependence of the current density with temperature is represented in Fig. 2.10b and Fig. 2.10c, respectively. A very weak dependence on temperature is obtained for V_a=9V, but a larger dependence is obtained at 24V, confirming our predictions.

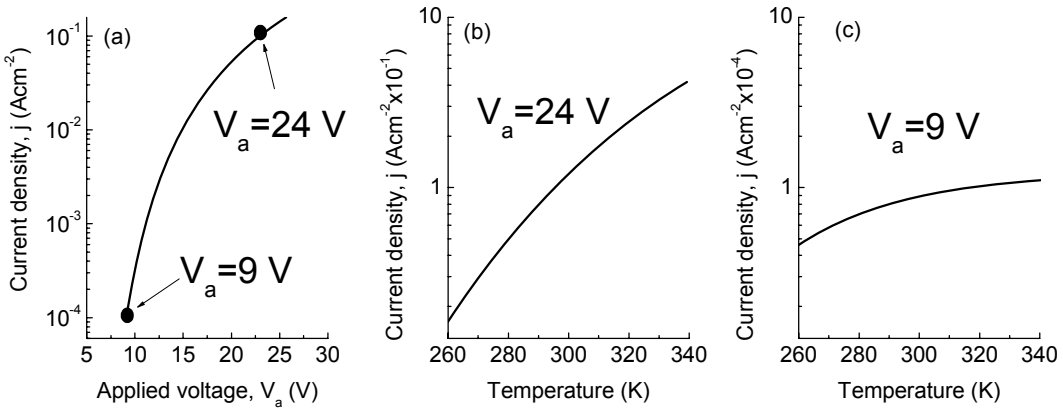

Figure 2.10. Current density curves for an ITO/MEH-PPV/Au organic diode, (a) as a function of the applied voltage, V_a; and as a function of the temperature for two applied voltages: (b) V_a = 24V, and (c) V_a = 9V. The current is strongly temperature dependent when V_a = 24V and the device response is controlled by transport requirements. The current is less sensitive to temperature variations between 260K and 340K when V_a = 9V and the device response is controlled by tunnel injection. The parameters of the sample used in these calculations are: L=120nm, ε=3.0, ρ_m=2×10^{21}cm^{-3}, mobility prefactor μ_o=91 cm^{2}V^{-1}s^{-1}, mobility activation energy Δ=0.44 eV, a barrier height φ_M = 0.63eV, and a uniform electric field E=$V_{contact}$/(L/3.5).

The behavior at low currents can be seen in experimental measurements for ITO/MEH-PPV/Au diodes [2.3]. A comparison between these experimental data (crosses) and our results (solid line) is presented in Fig. 2.11. The current density is depicted at a fixed applied voltage (V_a=17 V) as function of the temperature. We observe clearly a weak temperature dependence of the j-T characteristics.

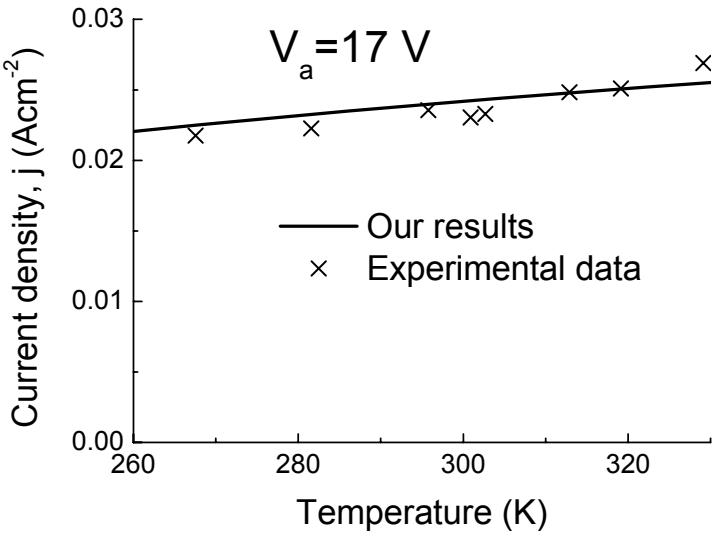

Figure 2.11. Comparison of the calculated current density as a function of the temperature (solid line) with experimental data measured in [3] (crosses) for an ITO/MEH-PPV/Au organic diode. The value of the applied voltage (V_a = 17V) is close to the tunneling onset, that correspond to a weak temperature dependence (see Figure 2.10). The sample parameters are: L=120nm, Area = 0.35cm^2, ε = 3.0, ρ_m =2×10^{21}cm^{-3}, μ_o=9.1×10^{-6}cm^{2}V^{-1}s^{-1}, Δ=0.025eV, a barrier height φ_M = 0.63eV, and a uniform electric field E=$V_{contact}$/(L/3.5).

This is due to the fact that the experimental data are taken in a low current regime, at which the device behavior is limited by tunneling instead of by SCLC transport, as discussed above.

Measurements in the high current range where the transport requirements control the slope of the *j-V* curve can be seen in [2.7] for ITO/ poly(*p*-phenylene vynilene) (PPV)/ Gold structures. A comparison of our numerical results (solid line) to the experimental data from [2.7] (symbols) is shown in Fig. 2.12. Again, a good agreement can be seen in this figure. In this case, a large dependence on temperature is observed, which is justified by a strong temperature-dependent mobility in the form of (2.16), with parameters μ_o=1.46 $cm^2V^{-1}s^{-1}$, Δ=0.366 eV.

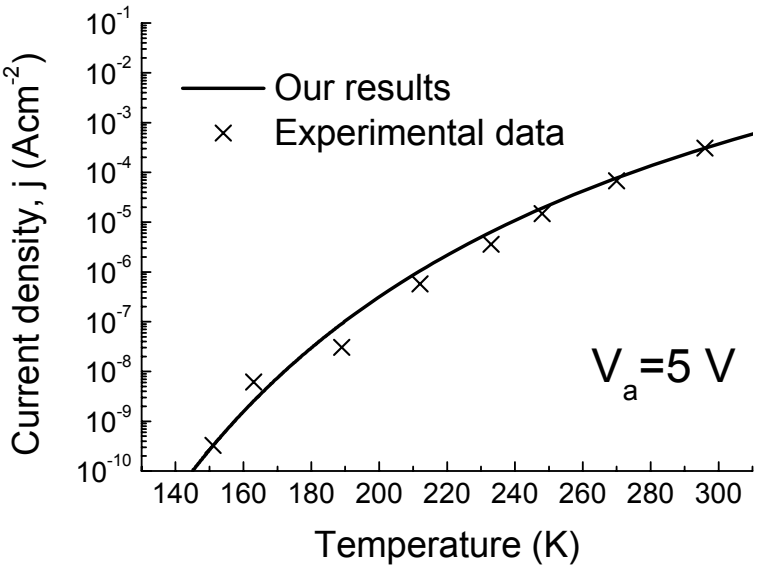

Figure 2.12. Comparison of the calculated current density as a function of the temperature (solid line) with experimental data measured in [2.7] (crosses), for an ITO/PPV/Au organic diode. The value of the applied voltage (V_a = 5V) is within the transport limited regime of the device. A strong temperature dependence due to a temperature activated mobility is observed as predicted in Figure 2.10. The sample parameters are: *L=275nm,* ε=3.0, $\rho_m=2\times10^{21}cm^{-3}$, mobility prefactor μ_o=1.46 $cm^2V^{-1}s^{-1}$, mobility activation energy Δ=0.366 eV, and a barrier height φ_M = 0.3eV.

2.4 Conclusions

We have developed a model for the charge transport in organic diodes, which includes charge injection, creation of a charge layer at the injecting electrode, and transport in the organic layer governed by charge drift. We have highlighted the importance of considering all the mechanisms that can take place in the transport of charge in organic diodes. In particular, we consider the combination of redox reactions with classical charge injection models such as thermionic emission and tunneling, and space-charge limited conduction in organic diodes.

We have proposed a method for the calculation of current-voltage (j-V) and current-temperature (j-T) curves. Two important cases have been derived from our model: a low voltage regime, in which the thermionic injection is dominant, and a high voltage regime, in which the tunnel injection is dominant. The combination of physical and chemical mechanisms in our model allows for the interpretation of a wide range of experimental data, and the model reproduces experimental data reported in publications from several research groups, including certain measurements that cannot be explained by taking into account only one phenomenon. An additional advantage of our model is the prediction of temperature dependent currents in the tunnel injection regime.

References

2.1. O. Marinov, M. J. Deen, B. Iniguez, "Charge Transport in Organic and Polymer Thin-Film Transistors: Recent Issues", *IEE Proc.-Circuits Devices and Syst.*, vol. 152(3), pp. 189–209, (2005).

2.2. B. de Boer, A. Hadipour, M. M. Mandoc, T. van Woudenbergh, and P. W. M. Blom, "Tuning of Metal Work Functions with Self-Assembled Monolayers", *Adv. Mater.*, vol. 17, pp. 621-625, (2005).

2.3. I. D. Parker, "Carrier tunneling and device characteristics in polymer light-emitting diodes", *J. Appl. Phys.*, vol. 75, pp. 1656-1666, (1994).

2.4. Y. Hirose, A. Kahn, V. Aristov, P. Soukiassian, V. Bulovic and S. R. Forrest, "Chemistry and electronic properties of metal-organic semiconductor interfaces: Al, Ti, In, Sn, Ag, and Au on PTCDA", *Phys. Rev. B.*, vol. 54, pp. 13748-13758, (1996).

2.5. N. F. Mott and R. W. Gurney, *Electronic Processes in Ionic Crystals*, Clarendon Oxford 1940.

2.6. P. W. M. Blom, M. J. M. de Jong, and M. G. van Munster, "Electric-field and temperature dependence of the hole mobility in poly(*p*-phenylene vinylene)", *Phys. Rev. B.*, vol. 55, pp. 656-659, (1997).

2.7. H. C. F. Martens, P. W. M. Blom, H. F. M. Schoo, "Comparative study of hole transport in poly(*p*-phenylene vinylene) derivatives", *Phys. Rev. B.*, vol. 61, pp. 7489-7493, (2000).

2.8. Y. Shen, M. W. Klein, D. B. Jacobs, J. C. Scott, and G. G. Malliaras, "Mobility-Dependent Charge Injection into an Organic Semiconductor", *Phys. Rev. Lett*., vol. 86, pp. 3867-3870, (2001)

2.9. S. R. Forrest, M. L. Kaplan, and P. H. Schmidt, "Organic-on-inorganic semiconductor contact barrier diodes. I. Theory with applications to organic thin films and prototype devices", *J. Appl. Phys.,* vol. 55, pp. 1492-1507, (1984).

2.10. M. Abkowitz, and D. M. Pai, "Comparison of the drift mobility measured under transient and steady-state conditions in a prototypical hopping system", *Phil. Mag. B*. vol. 53, pp. 193-216, (1986).

2.11. Z. P. Buffett, and W. R. Datars, "A lattice gas approach to conduction in organic material", *J. Phys.: Condens. Matter*, vol. 17, pp. 2919-2933, (2005).

2.12. H. Ishii, K. Sugiyama, E. Ito, and K. Seki, "Energy Level Alignment and Interfacial Electronic Structures at Organic/Metal and Organic/Organic interfaces", *Adv. Mater.*, vol. 11, pp. 605-625, (1999).

2.13. I. G. Hill, D. Milliron, J. Schwartz, and A. Kahn, "Organic semiconductor interfaces: electronic structure and transport properties", *Appl. Surf. Sci*., vol. 166, pp. 354-362, (2000).

2.14. L. Ke, R. S. Kumar, P. Chen, L. Shen, S. Chua, and A. P. Burden, "Au-ITO Anode for Efficient Polymer Light-Emitting Device Operation", *IEEE Phot. Tech. Lett.,* vol. 17, pp. 543-545, (2005).

2.15. I. H. Campbell, S. Rubin, T. A. Zawodzinski, J. D. Kress, R. L. Martin, and D. L. Smith, "Controlling Schottky energy barriers in organic electronic devices using self-assembled monolayers", *Phys. Rev. B*., vol. 54, pp. 14321-14324 (1996).

2.16. N. D. Lang, and W. Kohn, "Theory of Metal Surfaces: Charge Density and Surface Energy", *Phys. Rev. B.* vol. 1, pp. 4555-4568, (1970).

2.17. N. D. Lang, and W. Kohn, "Theory of Metal Surfaces: Work Function", *Phys. Rev. B*., vol. 3, pp. 1215-1223, (1971).

2.18. M. O. Bernard, M. Plapp, and J. F. Gouyet, "Mean-Field kinetic lattice gas model of electrochemical cells", *Phys. Rev. E.,* vol. 68(011604), pp. 1-14, (2003).

2.19. W. D. Gill, "Drift mobilities in amorphous charge-transfer complexes of trinitrofluorenone and poly-*n*-vinylcarbazole", *J. Appl. Phys.*, vol. 43, pp. 5033-5040, (1972).

2.20. H. Meyer, D. Haarer, H. Naarmann, and H. H. Hörhold, "Trap distribution for charge carriers in poly(paraphenylene) (PPV) and its substituted derivative DPOP-PPV", *Phys. Rev. B.* vol. 52, pp. 2587-2598, (1995).

2.21. R. . H. Fowler and L. Nordheim, "Electronic Emission in Intense Electric Fields", *Proc. R. Soc. London*, Ser. A 119, pp. 173-182, (1928).

2.22. Y. Qiu, Y. Hu, G. Dong, L. Wang, J. Xie, and Y. Ma, "H_2O effect on the stability of organic thin-film field-effect transistors", *Appl. Phys. Lett.*, vol. 83**,** pp. 1644-1646, (2003).

2.23. W. Tang, H. Shi, G. Xu, B. Ong, Z. Popovic, J. Deng, J. Zhao, and G. Rao, "Memory Effect and Negative Differential Resistance by Electrode-Induced Two-Dimensional Single-Electron Tunneling in Molecular and Organic Electronic Devices", *Adv. Mater.,* vol. 17, pp. 2307-2311, (2005).

2.24. M. J. Deen, M. H. Kazemeini, Y. M. Haddara, J. Yu, G. Vamvounis, S. Holdcroft, and W. Woods, "Electrical Characterization of Polymer-Based FETs Fabricated

by Spin-Coating Poly(3-alkylthiophene)s", *IEEE Trans. Electron Devices.,* vol. 51, pp. 1892-1901, (2004).

2.25. B. Lägel, M. M. Beerbom, B. V. Doran, M. Lägel, A. Cascio, and R. Schlafa,"Investigation of the poly[2-methoxy-5-(2´-ethyl-hexyloxy)-1,4-phenylene vinylene]/indium tin oxide interface using photoemission spectroscopy", *J. Appl. Phys.,* vol. 98(023512), pp. 1-7, (2005).

2.26. R. Schlaf, B. A. Parkinson, P. A. Lee, K. W. Nebesny and N. R. Armstrong, "Determination of frontier orbital alignment and band bending at an organic semiconductor heterointerface by combined x-ray and ultraviolet photoemission measurements ", *Appl. Phys. Lett.,* vol. 73**,** pp. 1026-1028 (1998).

2.27. A. Moliton, W. Rammal, and B. Lucas, "Field and temperature effects on the electronic mobility in Alq3 structures", *Eur. Phys. J. Appl. Phys.* vol. 33, pp. 175-182, (2006).

2.28. I. G. Hill, J. Hwang, A. Kahn, C. Huang, J. E. McDermott and J. Schwartz, " Energy level alignment between 9-phosphonoanthracene self-assembled monolayers and pentacene", *Appl. Phys. Lett.,* vol. 90**(**012109), pp. 1-3, (2007).

2.29. E. W. Forsythe, V.-E. Choong, T. Q. Le, and Yongli Gao, "Interface analysis of naphthyl-substituted benzidine derivative and tris-8-(hydroxyquinoline) aluminum using ultraviolet and x-ray photoemission spectroscopy", *J. Vac. Sci. Technol.* A17(6), pp. 3429-3432 (1999).

Chapter 3:
Injection and Transport of Charge Through the Contacts of Organic Transistors.

3.1 Introduction

Organic thin film transistors, OTFTs, have attracted considerable attention from many researchers during the last decade. A major application for these transistors is in low-end, high-volume microelectronics such as identification tags where mechanical flexibility and low-cost are necessary. These devices are also suitable for large-area flexible applications [3.1] and present low-cost, low temperature processing such as dipping or spin-coating technologies [3.2]. OTFTs are being considered for the drive electronics in liquid crystal display [3.3] and organic light-emitting diodes, and might also be applied to smart cards, gas sensors and other fields.

A key element in OTFTs research has been the organic semiconductor material itself. However, when Bürgi et al. [3.4] mapped the lateral potential distribution in the channels of OTFTs, they found that a substantial part of the externally applied drain−source voltage, V_{DS}, drops across the contact between the organic material and metal electrodes for source and drain, in particular between the source and the organic material. Thus, in addition to the limited drift in the organic film, there is one more limit for the charge flow in OTFTs owing to contact effects.

As a conclusion of potentiometry experiments, several authors [3.5], [3.6], [3.7] consider that the current finds two different resistive regions in the path from the source

to the drain, causing consequently a voltage drop at the contacts and a voltage drop along the intrinsic channel. The "parasitic" voltage drop at the contacts leads to a lowering of the effective bias voltage applied to the intrinsic drain-source channel of the transistor, and consequently, reduces the values for current and mobility [3.8], [3.9]. The relative importance of contact resistance increases with increasing charge carrier mobility in the organic layer or decreasing the channel length, L (L<1μm) [3.7], [3.8], [3.10]. The contact resistance may, therefore, become comparable to or even greater than the channel resistance in short channel devices or in devices with high mobility organic materials in the channel. Thus, it is very important to consider the contact effects when extracting the parameters of the transistors (i. e. mobility and threshold voltage) from the output characteristics of the device [3.6], [3.8].

Finding a model for OTFTs is not an easy task. The contact effects and other limiting mechanisms for the charge transport cannot be explained by the silicon metal−oxide−semiconductor field−effect transistor (MOSFET) model [3.8]. Uncommon output characteristics are associated with gate-voltage dependent contact resistances and mobilities [3.4], [3.5], [3.7], [3.11], [3.12], or with the topology of the transistor. Several studies [3.4], [3.8], [3.13] have shown that OTFTs with bottom contact (BC) design demonstrate inferior performance, compared to those with the top contact (TC) design. As a consequence of the problems cited above, the contact effects should be characterized.

As a consequence of all problems cited above, models are required to interpret the dependence of drain current on contact voltage [3.5]. Models devoted to reproducing current-voltage curves at the contacts of OTFTs show some controversies, mainly because two theories compete with each other: space-charge limited conduction (SCLC) or injection-limited conduction. Researchers who favor one theory neglect the other by

demonstrating problems to reproduce certain dependences of the current with the applied voltage, the temperature, dimensions of the device or different kinds of contacts. The limitations of the reported approaches have their origin in the fact that they focus only on a particular phenomenon and therefore explain only certain I_D-V_C dependences. To address these limitations and provide a consistent description of the phenomena present in the contacts of OTFTs, we apply the model for diodes in the previous chapter to the contact effects in OTFTs. As described in chapter 2, the voltage drop at the contact, V_C, is the superposition of different components. Each component is related to a different mechanism in the contact: injection, redox reactions at the interface and drift in the adjacent organic material.

This chapter is organized as follows: In section 3.2, we review different models, found in the literature, which report on the contact effects in OTFTs. The strengths and weaknesses of each model are discussed. In this section, we adapt the model presented in the previous chapter to the contacts of OTFTs. In section 3.3, we focus on the characterization techniques related to the proposed model, by reviewing and discussing the different characterization approaches. We also propose a method for extracting contact effects when a set of transistors with different channel lengths is not available. The characterization techniques allows for extracting the parameters of the transistor and the contact voltage drop from the output characteristics. Finally, a validation of our model by the characterization of several OTFTs is presented in section 3.4.

3.2 Modelling of the Contact Effects

The objective, when modeling the contacts of OTFTs, is the reproduction of the I_D-V_C curves and their dependences on bias voltages, temperature and material parameters [3.4], [3.14], [3.15], [3.16], [3.17]. The two main theories used for the explanation of contact effects in OTFTs are the injection-limited conduction and space-charge limited

conduction (SCLC) theories. A review of models based on these theories is presented below.

3.2.1 Injection Limited Conduction

Baldo and Forrest [3.18] studied the transport of charge in a variable thickness layer of tris(8-hydroxyquinoline) aluminum (Alq3) sandwiched between two metal electrodes. In order to explain their experimental curves, they proposed that the transport is injection-limited and that the injection is limited by charge hopping where interfacial dipoles play a crucial role because they may alter the effective injection barrier. They eliminated other models, as explained below. At a constant electric field, the bulk-limited models predict a dependence of current density, *J*, on the thickness of the organic layer, *d*, according to $J \propto 1/d^x (x \geq 1)$. This dependence was not observed in [3.18], and therefore they eliminated the bulk-limited model. Another reason for ruling out bulk-limited models is that they do not predict the different characteristics for different cathodes that were observed in [3.18]. Baldo and Forrest [3.18] also eliminated injection models that depend only on the energy barrier at the interface because the cathode dependence of current-voltage characteristics at low temperatures is substantially reduced. They proposed that the injection is limited by charge hopping where interfacial dipoles play a crucial role as they may alter the effective injection barrier. However, they left an open question on the origin of the interfacial dipoles that lead to a lowering of the interface energy barrier.

Another proposal of injection limited model is in [3.16], [3.19]. The model in [3.16], [3.19] is based on thermionic emission with diffusion-limited injection currents, and it was used in [3.10] to interpret contact resistances in bottom contact poly(3−hexylthiophene) (P3HT) OTFTs with Au as source and drain contact material. This model was dismissed in [3.20] because it could not reproduce the dependence with

the temperature for OTFTs having high injection barriers between the organic layer and source/drain electrodes, such as the contacts in OTFTs formed between Cr or Cu with P3HT [3.20]. In order to reproduce the dependence with the temperature for OTFTs with high injection barriers, a more sophisticated model of hopping injection into a disordered density of localized states was used later [3.20].

3.2.2 Space Charge Limited Conduction

In TFTs with relatively small contact effects, the contact resistance is found to be dominated by the mobility of the polymer [3.4]. This suggests that bulk drift dominates in the contact. On the other hand, small contact effects produce a voltage drop in the contact that depends almost linearly on the current flowing through the contact, i.e. nonlinear effects in the output characteristics of the transistor are nearly negligible (Fig. 2 in [3.20]). This means that bulk drift models like the classical Mott−Gurney law [3.21], [3.22], where the dependence of the current density with the applied voltage is non-linear, could not reproduce experimental characteristics of the contacts of OTFTs [3.7], [3.20].

3.2.3 Compact Model for Contacts in OTFTs

None of the aforementioned models can individually explain certain experimental data. The linearity of the current-voltage curves at the contacts, I_D-V_C, in [3.7], [3.20] can be explained neither by the drift model in [3.21], [3.22] nor by the injection-limited models [3.16], [3.18], [3.19]. The drift and the injection-limited models have been used for contacts with nonlinear responses, but not for devices showing linear I_D-V_C curves. If the contact region thickness increases over 100nm, transport must eventually become bulk limited [3.18] and the injection models have to be combined with drift models. Consequently, some combination of the models should be studied. In addition, it is also

necessary to understand the chemistry at the metal/organic interface and the physical origins of the interface dipoles that lead to a lowering of the interface energy barrier [3.18].

So, we find as appropriate, a compact model for contacts in OTFTs which takes into account the different phenomena reported in the contacts of OTFTs.

A unified model was developed in the previous chapter, and published in [3.23], to explain the transport in organic diodes. Considering that the same principles for the contact effects in organic diodes are valid for other organic devices [3.5], this model is now applied to the depleted region located between the source and the accumulation layer in the organic material of OTFTs. This region includes the source contact and a low conductivity region [3.24] close to it (Fig. 3.1).

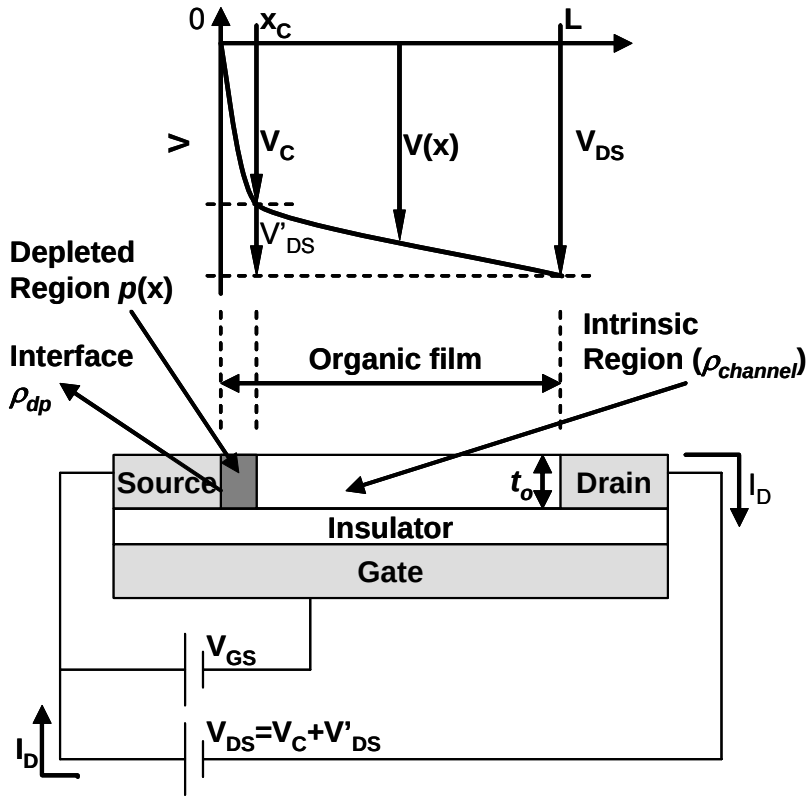

Figure 3.1. Separation of the channel of a bottom contact organic transistor in two regions: the contact region [0, x_C] modeled by a voltage drop V_C and the intrinsic channel [x_C, L].

There is not only electrical evidence of the depleted region (as was demonstrated by Bürgi by means of scanning probe potentiometry [3.4]) but also structural evidence of this region as was found in [3.25]. They have detected a transition region from a large grain pentacene, in the bulk of the channel of Au-pentacene OTFTs, to a microcrystalline form at the interface between the metal electrode and the organic film. The voltage drop at the drain contact is much less important than the voltage drop at source, as supported by scanning probe potentiometry [3.4] and will therefore be ignored.

Our compact model assumes that same phenomena detailed in previous chapter for diodes, take place in charge transport through the depleted region of the OTFT:

- Charge carriers pass a potential barrier at the contacts.
- Ions are created at the electrodes by redox reactions in the organic material. These ions form charged dipoles which modulate the injection barrier.
- Drift of charge carriers in the bulk of the contact region.

Thus, to maintain a current I_D, the contact voltage, V_C, is shared by voltages required for carrier injection through the barrier, $V_{injection}$, for ion formation (redox reactions), V_{red}, and for charge drift, V_{drift}. The relationship between the contact voltage V_C and the current through the structure is described by the equation:

$$V_C = V_{injection}(I_D) + V_{red}(I_D) + V_{drift}(I_D). \tag{3.1}$$

Expressions for the different components in (3.1) were already presented in the previous chapter. However, the variables are defined here according to the structure and geometrical dimensions of an OTFT (Fig. 3.1). We review the calculations of the compact model adapted to this new situation in equations (3.2), (3.3), and (3.4) below.

The voltage for the ion formation V_{red}, according to Nernst equation [3.23] is:

$$V_{red} = \Phi + V_t(T)\ln(\rho_{dp}/\rho_m), \tag{3.2}$$

where ρ_{dp} is the value of the ion density forming the dipoles at the interface between the metal and the organic material, Φ is a constant which depends on the materials involved in a given redox reaction, ρ_m is the molecular density of the organic material, and $V_t(T) \equiv kT/e$ is the thermal voltage, where T is the absolute temperature, k=1.38×10^{-23}J/K is Boltzmann's constant, and e=1.6×10^{-19}C is the magnitude of the electron charge.

The voltage required for the transport across the contact region is calculated assuming that the charge transport is due to the drift of positive charges in a space-charge region with charge density at the interface $p(x=0)=p(0)$ (we focus on p-type OTFTs). In the previous chapter, it was developed the calculation of the voltage drop associated with the charge drift imposing a finite value for the charge density at the interface. The I-V relation is (2.15):

$$V_{drift} = \frac{2}{3}\left\{\frac{2J}{\varepsilon\mu}\right\}^{1/2}\left\{\left[x_c + x_p\right]^{\frac{3}{2}} - \left[x_p\right]^{\frac{3}{2}}\right\}, \quad x_p \equiv \frac{J\varepsilon}{2e^2\mu\left[p(0)\right]^2}, \qquad (3.3)$$

where $J=I_D/S$ is the current density, S is the cross section of the metal/organic contact, $S=t_o \times W$, t_o is the thickness of the organic layer and W the channel width of the OTFT, x_c is the contact length equal to the length of the depleted region as shown in Fig. 3.1, ε is the permittivity of the organic material, μ is the mobility of the carriers, the parameter x_p is a characteristic length (from contact interface toward organic film), in which the charge density $p(0)$ at the metal/organic interface decays to p(0)/$\sqrt{2}$. In a first-order of approximation, $p(0) \equiv \rho_{dp}$, where ρ_{dp} is the ion density in (3.2) for the barrier reduction, V_{red}.

Equation (3.3) allows for the incorporation of a variety of mobility models for the charge carriers, e. g. a variable range hopping (VRH) model [3.15] or band-transport model [3.26].

The voltage required for the injection, $V_{injection}$, could be evaluated using the injection models [3.16], [3.18], [3.19], [3.23], [3.27] discussed in section 3.2.1. In general, charge injection through metal−organic junction can be due to thermionic emission and tunneling [3.23]. However, in OTFTs, the electric field at the contact is not very high. Therefore, we consider a thermionic-emission-like expression where the barrier height, φ_M, is modulated by a term associated to redox reactions, V_{red}:

$$\begin{aligned} I_D &= A^* T^2 S \exp\left(\frac{-\varphi_M}{kT}\right)\exp\left(\frac{V_{red}}{V_t(T)}\right)\left[\exp\left(\frac{V_{injection}}{\eta V_t(T)}\right)-1\right] \\ &= I_S\left[\exp\left(\frac{V_{injection}}{\eta V_t(T)}\right)-1\right], \end{aligned} \tag{3.4}$$

where A^*= 120Acm^{-2}K^{-2} is the Richardson´s constant, φ_M is the height of the barrier between the source metal and the organic layer, I_S is the saturation current and η is ideality factor of the junction. As mentioned in the previous chapter, the barrier height, φ_M, is calculated as the difference between the metal work function and the organic material´s highest occupied molecular orbital (HOMO) [3.1], [3.6], [3.17], [3.28]. V_{red} is the barrier reduction owing to dipoles at the interface between the source contact and the metal [3.18]. The barrier reduction is accounted by V_{red}. Larger V_{red} increases the saturation current I_S by exp(V_{redox} /V_t(T)), see again (3.4).

3.3 Characterization Techniques

An important problem in OTFTs research is the separation of contact effects from the characteristics of the intrinsic transistor. The separation is not a trivial task because the contacts effects interfere with other dependences in OTFTs [3.8]. For example, the mobility and the threshold voltage extracted by commonly used techniques based on the MOSFET model are influenced by the contacts [3.24] and, as a result, the OTFT data needs further processing. In this section, we discuss approaches to extract the current

versus voltage curve at the contact, I_D-V_C, the threshold voltage, V_T, and the charge carrier mobility, μ.

It was considered [3.5], [3.13], [3.29] that the mobility and/or contact resistance are gate-voltage dependent. However, different parameters are attributed to be dependent on the gate voltage as discussed below.

For Au-sexithiophene OTFTs, a method assuming a constant contact resistance and a gate voltage-dependent mobility was developed to extract the mobility from the transfer characteristics and to estimate values for the threshold voltage and contact resistance [3.29], [3.30].

For Au-pentacene OTFTs, a model with a gate voltage-dependent mobility and highly nonlinear drain and source contact resistances was proposed to simulate the transport characteristics [3.13].

On the other hand, in OTFTs based on polyfluorene F8T2, which makes a non-ohmic contact with Au, the mobility has been assumed constant and the nonlinear current-voltage relation at the source has been considered dependent on the gate voltage [3.5]. The contact resistance was extracted from the output characteristics of transistors with different channel lengths, and the contact current was found to be exponentially related to the contact voltage. It is also shown in [3.6] that the method can be used to simultaneously extract the mobility and the I_D-V_C curve. We will show shortly that an alternative method to extract the I_D-V_C curves and mobility can be used when a set of devices with different channel lengths is not available.

Overall, the procedures for extraction of contact characteristics can be grouped in two approaches: by variation of channel length or by variation of gate bias voltage. These are now described.

3.3.1 Set of Transistors with Different Channel Lengths

This procedure is based on assumption that the channel of an OTFT, such as the p-channel bottom-contact configuration depicted in Fig. 3.1, can be split into two regions: a contact region and an intrinsic TFT region. With this assumption, the total source-drain voltage V_{DS} is therefore split into a channel component V_{DS}' and a voltage dropped at the contacts V_C. It is supported by scanning probe potentiometry [3.4], that V_C is mainly dropped at the source contact. By using the gradual-channel approximation and after integration of the potential along the channel, the current of OTFTs is obtained as [3.5], [3.6], [3.24]

$$I_D = \mu W C_{ox} / (L - x_c)\{(V_{GS} - V_T)(V_{DS} - V_C) - (V_{DS}^2 - V_C^2)/2\}, \quad (3.5)$$

where C_{ox} is the gate capacitance per unit area, and the mobility might be unknown, but is constant at a given gate voltage.

When identically processed transistors with different channel lengths (but the same channel width) are available, the $I_D - V_{DS}$ curves are measured at a given gate-source voltage V_{GS} for each transistor. The corresponding $I_D - V_C$ is calculated from Eq. (3.5) for all the different transistors. Assuming that the contact and channel transport are identical in different transistors (independent of L), the correct value of μ would make all the different $I_D - V_C$ curves to overlap when the different samples have the same width.

This technique has been used for different length OTFTs based on several organic materials [3.6], [3.12], [3.24], [3.30] in BC configuration. It has been shown that both the mobility and the contact resistance are gate voltage dependent [3.6], [3.12], [3.24]. This characterization technique, however, has two limitations [3.7]. One is that a series of devices with different channel lengths, but otherwise identical, has to be available. Another is the channel transport properties in different devices might not be

exactly the same. In such cases, we propose to use the alternative characterization technique with variable gate biasing, given below.

3.3.2 Set of Characteristics of a Single Transistor Biased at Different Gate Voltages

In the case when transistors with different channel lengths are not available or the transport depends on L, we propose a method based on the output characteristics at different bias conditions. The details of the procedure to extract the I_D-V_C curves and the mobility are the following.

First, initial estimates for the threshold voltage and the mobility are made by means of the MOSFET model [3.7], [3.24] by fitting a transfer characteristic in saturation regime. The initial estimates are the so-called apparent threshold voltage, V_{AT}, and apparent mobility, μ_A [3.7], [3.24].

Second, it is observed that the contact effects only slightly increase the threshold voltage of the OTFT [3.5], therefore, $V_T \approx V_{AT}$, and the initial value for the threshold voltage is assumed also as a final value.

Third, the mobility and the voltage drop at the contact are extracted from the output characteristics, by iterative procedure using eq. (3.5). The procedure accounts for the following facts: (i) both the mobility and the contact voltage are gate voltage dependent, and (ii) the apparent mobility, μ_A, is lower than the mobility, μ, in intrinsic OTFT because μ_A includes contact effects.

To set up the iterative use of eq. (3.5), we also define a parameter $\alpha \equiv V_C/V_{DS}=[R_C/(R_{ch}+R_C)]$, which accounts for the ratio between the contact resistance and the channel resistance [3.24].

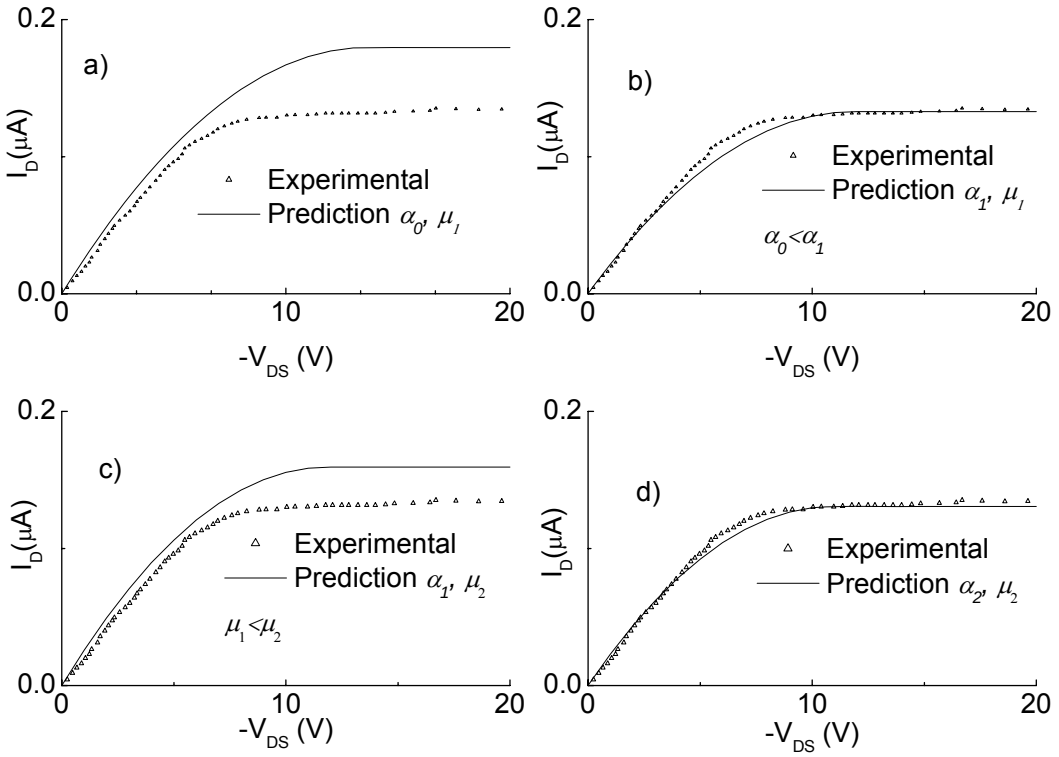

Figure 3.2. Iterative procedure to fit output characteristics in an OTFT (symbols) with (5) (solid lines). For clarity, only a sample curve measured at a given V_{GS} is shown. For other values of $V_{GS} > V_T$ the graphs are similar. (a) First step of the iteration, reproduction of experimental data in the linear region. Calculation with α_0=0 and μ_1 in (5) (b) Second step of the iteration, reproduction of experimental data in the saturation region. Calculation with α_1 and μ_1 in (5). (c)(d) Calculation of the second iteration as described in (a)(b) with the values of this iteration: α_2 and μ_2.

The iterative procedure is performed by using the output characteristic at given gate voltage, and then repeated for all gate voltages. The procedure is illustrated in Fig. 3.2 and begins with the initial values mentioned above, α_0=0, and $\mu_0=\mu_{AT}$. A new value μ_1 for mobility is obtained by fitting (3.5) to the experimental output characteristics in the linear regime (varying the value for mobility), as shown in Fig. 3.2a. Next, a new value α_1 is obtained by fitting (3.5) to the experimental output characteristics in the saturation regime (using μ_1 and varying α), as shown in Fig. 3.2b. Then, the above two fitting procedures are repeated alternatively, obtaining the values μ_i and α_i after each loop of number (i) of the iteration. The results from fitting (3.5) in linear and saturation

regimes in the second loop (i=2) are shown in Fig. 3.2c and Fig. 3.2d respectively. The above two fitting procedures are repeated until a good agreement with experimental data in linear and linear-saturation transition regions, is reached.

The convergence of the method has been proven good. For example, see again Fig. 3.2d. After the second iteration, the model characteristic is almost identical with the measured. Also, as another criterion, it is illustrated later in section 3.4.2 that the above procedure obtains values for mobility that increase with the gate voltage and values for contact resistance that decrease with the gate voltage, as repeatedly observed in experiments, e.g. in [3.24].

3.4 Validation of the Model by Characterization of Devices

In this section, we demonstrate that the model presented in this chapter interprets consistently I_D-V_C curves of different OTFTs with output characteristics impacted by contact effects. The examples include both characterization methods, set of transistors with different channel lengths at constant gate voltage and set of characteristics of a single transistor biased at different gate voltages.

We chose experimental data for OTFTs with bottom contact (BC) configuration, because they are easier to fabricate [3.13], [3.25]. Also, BC OTFTs are more susceptible to contact effects than the top contact (TC) configuration owing to area of the contact [3.5].

Since our model uses several material parameters, the electrode work function and the energy levels of the organic semiconductors are collected from the literature [3.20], [3.23], [3.28], [3.31] and are summarized in Tables 3.1 and 3.2. We consider that the relative permittivity for organic materials is around 3 ($\varepsilon_r \approx 3$) as reported for many

materials in [3.23], [3.29], the molecular density is ρ_m=2×10^{21} cm^{-3} as reported in [3.23], and the contact length x_c is around ≈100nm as deduced by non-contact scanning-probe techniques [3.4]. The mobility in the organic materials is extracted by the characterization techniques detailed in section 3.3, and by also using geometrical dimensions reported along with the experimental data in the literature.

Table 3.1. Electrode work function of the metals referred to in this chapter.

Electrode	**Work function (eV)**	**Reference**
Gold (Au)	4.9–5.47	[3.23]
Chromium (Cr)	4.5–4.8	[3.31]

Table 3.2. Properties of the organic semiconductors referred to in this chapter.

Organic film	**HOMO (eV)**	**Reference, Year**	**Metal−Organic interface**		
			Interface	**Barrier height (eV)**	**Nernst potential**
F8T2	5.5	[3.28], 2004	Au/Cr−F8T2	0.68	Φ=0.22 V
Pentacene	4.8–5.0	[3.23], 2005	Au−Pentacene	0.1	Φ=0.39 V
P3HT, P3HDT	≈5.2	[3.20], 2005	Au−P3HDT	<0.4	Φ=0.30 V

3.4.1 Validation by the Method Using Set of Transistors with Different Channel Lengths

The extraction method is detailed in section 3.3.1. It is applied to output characteristics reported in Fig. 5a in [3.7] for BC pentacene OTFTs with Au contacts, channel width W=270 μm and channel lengths L=2, 10, and 20 μm. The extracted I_D-V_C curves are shown in Fig. 3.3a with symbols. For a mobility μ=0.8cm^{2}V^{-1}s^{-1}, the I_D-V_C curves converge in a straight line reproduced by the compact model. The calculations of the compact model are detailed below.

The barrier height in these OTFTs is low, φ_M =0.1eV, and the experimental currents are quite below the saturated current, $I_D^{exp} << I_S=A^*T^2S\cdot\exp(-\varphi_M/kT)$ which results in small injection and redox voltages. The dominant phenomenon in this contact is therefore drift, and the voltage drop at the contact, V_C in (3.1), is: $V_C \approx V_{drift}$. As a result of these particular conditions, the electrical characteristics of these contacts are represented by linear I_D-V_{drift} curves, which can be deduced from (3.3), as explained below.

If the characteristic length x_p is a few times larger than the contact length x_c, we can expand in a Taylor series, $x_p^{3/2}\left\{\left[1+\left(x_c/x_p\right)\right]^{3/2}-1\right\}=3/2\,x_c x_p^{1/2}+...$, which reduces (3.3) to Ohm´s law

$$I_D \approx e\,S\,p(0)\,\mu\frac{V_{drift}}{x_c}. \tag{3.6}$$

According to our model, the charge density at the interface, $p(0)$, equals to the value of the ion density, ρ_{dp}, and the prediction is calculated with (3.2) to (3.6). After the calculation, V_{red}~2mV is verified to be much smaller than V_{drift} >100mV.

In the comparison above, we have studied an ohmic contact in OTFTs and we have demonstrated a reproduction of these contacts with the compact model. Next, we will

study non-ohmic contacts in OTFTs, particularly the contacts effects between chromium/gold electrodes and F8T2 with data from [3.5].

The I_D-V_C curves are extracted from the output characteristics given in Fig. 2 of [3.5] for transistors with different channel lengths. For a mobility $\mu=6\times10^{-3}cm^2V^{-1}s^{-1}$, the I_D-V_C curves converge, as shown in Fig. 3.3b with symbols. The compact model prediction (solid line) together with the injection component (dotted line) and the drift component (dashed line) are also depicted in Fig. 3.3b

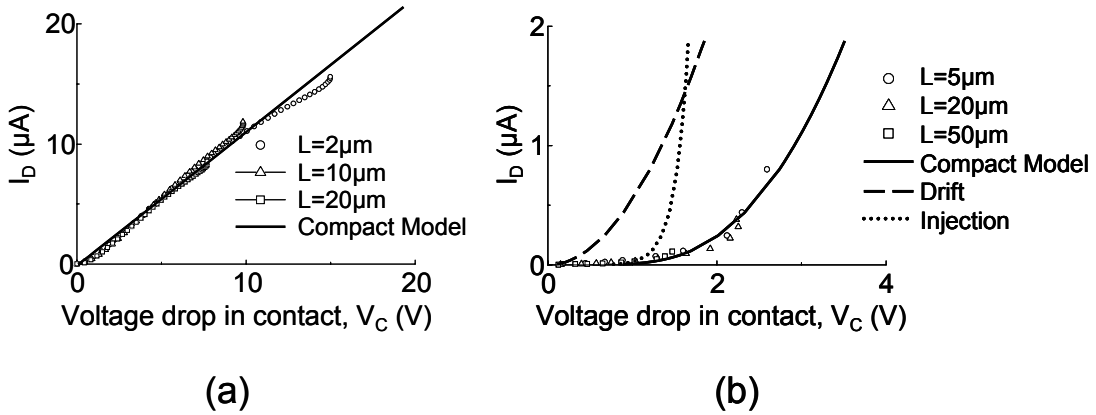

Figure 3.3. I_D-V_C curves extracted with equation (3.5) and output characteristics, as described in section 3.3.1. (a) Experimental I_D-V_C curves from Au−pentacene OTFTs data in [3.7] (symbols). The different channel lengths are L=2, 10 and 20 μm, W=270 μm, x_C=100nm, μ=0.8cm^{2}V^{-1}s^{-1}, the SiO_2 gate insulator thickness is 333nm, and $V_{GT}=V_{GS}-V_T=20V$. The barrier height between gold and pentacene is very low, making $V_{redox}\approx0$ and $V_{injection}\approx0$. The compact model prediction (solid line) from (3.1) is approximated by the drift term, (3.6), and reproduces well the experimental data. The thickness of the organic layer is t_O=50nm and the Nernst potential is Φ=0,39V. (b) Experimental I_D-V_C curves from Au/Cr−F8T2 OTFTs data in [3.5] (symbols), the different channel lengths are L=5, 20 and 50 μm, W=1000 μm, x_C=100nm, μ=0.006cm^{2}V^{-1}s^{-1}, the SiO_2 gate insulator thickness is 200nm and $V_{GT}=V_{GS}-V_T$=15V. The drift term (dashed line) is calculated from (3.7) to obtain a parallel displacement with the experimental data, the comparison between (3.7) and the general drift term in (3.3) suggests that the redox voltage is small. The injection term (dotted line) is then calculated from (3.4) and the compact model prediction (solid line) is the addition of the three terms. The barrier height is φ_M=0.68eV, the thickness of the metal electrodes is t_O=100nm and the Nernst potential is Φ=0.22V.

A nonlinear response of the contact can be observed. In [3.5], they have neglected the drift of the charge in the contact and proposed a diode-type relation as sufficient to reproduce the experimental measurements. As a result, they have obtained an unusually high value of the ideality factor, η=20. The compact model can describe non-ohmic contacts by using the terms related to charge drift and injection processes,

(3.3) and (3.4), with a lower value of the ideality factor. A non-linear relation between the current and voltage in the drift term occurs when the characteristic length x_p is much smaller than the contact length x_c, and (3.3) reduces to Mott−Gurney law [3.21], [3.22]

$$I_D \approx \frac{9}{8}\varepsilon\mu S\frac{(V_{drift})^2}{(x_c)^3}. \tag{3.7}$$

V_{drift} from (3.7) is shown by dashed line in Fig. 3.3b, illustrating a parallel displacement (along the x-axis) with the experimental data (symbols) for the set of three chromium/gold−F8T2 OTFTs [3.5]. This parallel displacement suggests that the drift term calculated from (3.7) is appropriate for this set of data.

The fact that the drift term is characterized with (3.7), implies a short characteristic length x_p which is obtained when $p(0)$ is large or the redox voltages are small, according to (3.2) and (3.3). The redox term is therefore small in these chromium/gold−F8T2 OTFTs, $V_{redox}\approx 0$. The small contribution of the redox reactions in these contacts make the injection and the drift the main contribution to the voltage drop in the contact, $V_C \approx V_{injection}+V_{drift}$ according to (3.1). A similar parallel displacement, between a space-charge-limited current and experimental currents, can be seen in Fig. 3.1 of [3.19]. For that case, the authors also proposed the injection as a displacement between experimental data and the space charge limited conduction.

3.4.2 Validation by the Method Using a Set of Characteristics of a Single Transistor Biased at Different Gate Voltages

Here, we are applying the procedure from Section 3.3.2 to extract the mobility and the contact voltage drop from the output characteristics of a single transistor at different gate voltages. We consider the output characteristics measured in poly(3−hexadecylthiophene) (P3HDT) transistors [3.24] (symbols in Fig. 3.4).

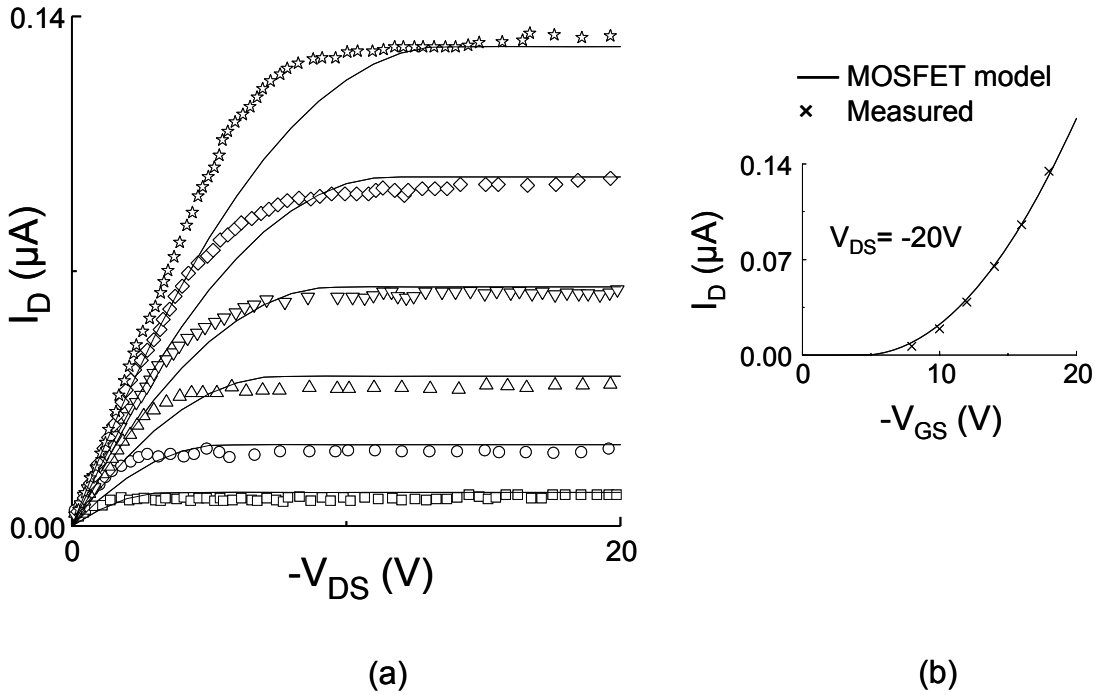

Figure 3.4. (a) Output characteristics of an Au-P3HDT bottom contact transistor [3.24] at V_{GS}=−8V, −10V, −12V, −14V, −16V, and −18V from the bottom to the top. Symbols represent experimental data. Lines represent the fitting with the simple MOSFET model without contact effects (μ_A=5.5×10^{-5}cm^2/Vs, V_{AT}=−4.4 V). As shown, the model deviates from the experimental data. The details for the samples are: thermally grown SiO_2 (≈200nm), channel width W=1.5 cm (multi-finger configuration), and channel length L=10 μm. The polymer film is 7nm thick and it was deposited by spin-coating. (b) Transfer characteristics at V_{DS} =−20V, used for an initial estimation of the mobility and the threshold voltage before iterations (the symbols represent experimental data and the line is the fitting with the simple MOSFET model).

When the initial values for apparent mobility μ_A=5.5×10^{-5} cm^2/Vs, α=0 and threshold voltage V_{AT}=−4.4 V, are used in the MOSFET model, a reasonable fitting can be obtained in the saturation region, as shown by solid lines in Fig. 3.4. However, the disagreement between this simplified model and the experimental curves in the linear regime is clear, when neglecting the effect of contacts.

Taking the above initial values for μ_A and V_{AT}, the iterative procedure defined in Section 3.3.2 is applied to determine the contact effects from the output curves of this OTFT. After the iteration procedure, the values of the intrinsic mobility, μ, and the contact voltage drop, V_C are obtained. Substituting μ and V_C in (3.5), a very good fit at each gate voltage is obtained, as depicted in Fig. 3.5a, in both saturation and linear regimes.

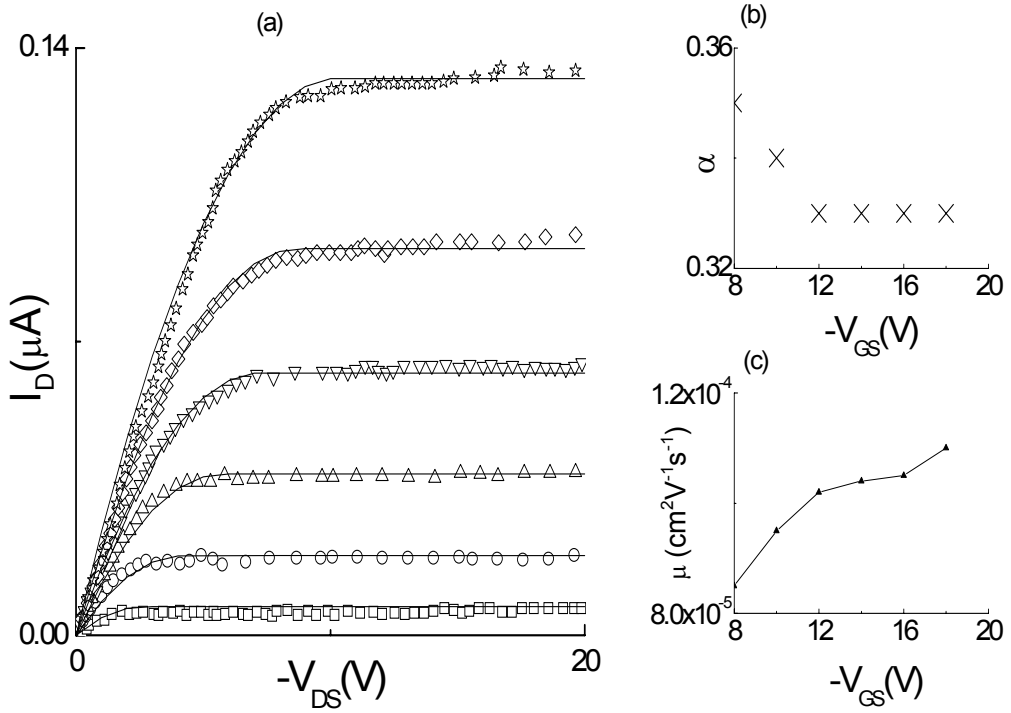

Figure 3.5. (a) Experimental I_D-V_{DS} curves from Figure 3.4 (symbols) and calculations of the I_D-V_{DS} curves (solid lines) taking into account the contact effects. The calculations are according to (3.5) with parameter $\alpha=V_C/V_{DS}=[R_C/(R_{ch}+R_C)]$ in Fig. 3.5b and mobility in Fig. 3.5c as function of V_G.

The values for $\alpha=V_C/V_{DS}=[R_C/(R_{ch}+R_C)]$ and μ are given in Fig. 3.5b and 5c, respectively. Note that the mobility increases with the gate voltage as reported in the literature for different OTFTs [3.11], [3.15]. The parameter α, that accounts for the ratio between the contact resistance and the channel resistance $\alpha=[R_C/(R_{ch}+R_C)]$, shows that the contact resistance decreases with the gate bias voltage. A decrease of the contact resistance, by charging the traps in the depleted region and increasing the concentration of free carriers, have been reported in the literature, by means of increasing the gate voltage [3.4] or by photogeneration [3.24], [3.32]. The decrease of the contact resistance is explained by the increase in the induced charge carriers throughout the depleted region of the contact. The depleted region of the contact is rich in defects and they cause the injected charge to get trapped, limiting the current flowing through the device. Thus, the greater the level of trapped charge by increasing the gate voltage or by illumination,

the easier for the injected charge to travel across the depleted region without being trapped.

Using the values of α and μ given in Fig. 3.5b and 3.5c, the contact I_D-V_C characteristics of the Au−P3HDT OTFT are finally calculated. These I_D-V_C curves are shown in Fig. 3.6 with symbols and reveal that the contact in Au-P3HDT OTFTs is ohmic. The prediction of the Unified Model is shown with solid lines in Fig. 3.6, it is calculated with (3.6) and reproduces the experimental data in the linear regime.

An ohmic contact is expected owing to the small barrier height $\varphi_M < 0.2eV$ between the gold electrodes and the P3HDT film. For this small barrier height, the contact voltage is mainly a result of the drift of charge, by the reasons discussed in the first part of the previous subsection, 3.4.1. The redox and the injection terms are small compared to the drift term. That is why the prediction of the Unified Model, calculated from eq. (3.6), reproduces the experimental data.

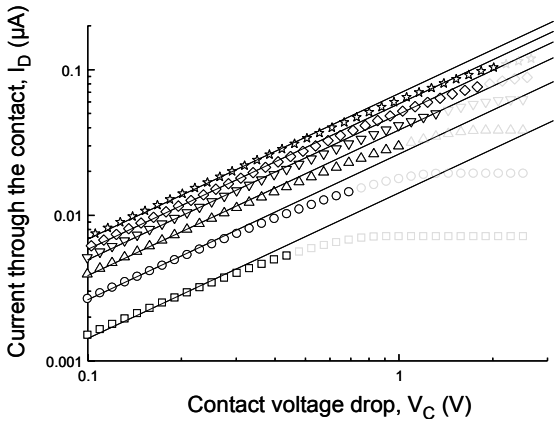

Figure 3.6. Contact I_D-V_C characteristics of Au−P3HDT OTFT from [3.24]. Symbols are extracted values from the output characteristics at different gate voltages after using the iteration method. Lines are calculated with the ohmic prediction of the compact model, equation (3.6). From bottom to top, V_{GS}=−8V, −10V, −12V, −14V, −16V, −18V and ($V_{redox}-\Phi$)=−0.316V, −0.303V, −0.295V, −0.289V, −0.285V, −0.282V. See figs 3.4 and 3.5 for fabrication and electrical parameters. Gray symbols illustrate saturation regime of operation of TFT, in which the condition for use of (3.5) are violated.

3.4.3 Limits of Validity

The divergence between the experimental I_D-V_C curves and the prediction of the compact model near the saturation region points out the voltage range where our procedure is valid. This disagreement is due to the operation of the transistor in the saturation regime, where the conditions for the approximation $V_C=\alpha V_{DS}$ used in the extraction procedure are violated. It can be see from (3.5) that the extraction of I_D-V_C curves is valid in the linear regime. The reason is that the gradual channel approximation is used in order to relate the drain current to the terminal voltages ($I_D= I_D(V_{GS}, V_{DS})$). Once this relation is defined, the contact effects are separated from the characteristics of the intrinsic transistor, $V_{DS}= V_C +V'_{DS}$.

This procedure, used in the linear regime, would still be valid in subthreshold or saturation regimes if proper expressions for the $I_D=I_D(V_{GS}, V_{DS})$ curve are employed. In any of these three regimes, our model might be applied in order to reproduce the extracted I_D-V_C curves. No limits are imposed on our model outside the linear regime as the mobility and the charge density are the only variables in our model. Moreover, the mobility is not limited to a given voltage range because our model allows for the incorporation of different mobility models.

3.5 Conclusions

A compact model for the injection, interface dipoles and transport of charge through contacts in organic transistors has been presented. The combination of different physical phenomena in the model allows for the interpretation of a wide range of experimental data. Our model explains linear and non-linear current-voltage curves at the contacts of organic transistors extracted by different characterization methods.

The ability of this compact model to fit various data for nonlinear contacts can help to obtain deeper insights for the details and physical origin of the charge injection in organic devices, simultaneously providing a link to compact modeling.

References

3.1 C. D. Dimitrakopoulos, P. R. L. Malenfant, "Organic Thin Film Transistors for Large Area Electronics", *Adv. Mater.*, vol. 14, no. 2, pp. 99–117, (2002).

3.2 M. G. Kane, J. Campi, M. S. Hammond, F. P. Cuomo, B. Greening, C.D. Sheraw, J. A. Nichols, D. J. Gundlach, J. R. Huang, C. C. Kuo, L.Jia, H. Klauk, T. N. Jackson, "Analog and digital circuits using organic thin-film transistors on polyester substrates", *IEEE Electron Device Lett.*, vol. 21, no. 6, pp. 534–536, (2000).

3.3 C. D. Sheraw, L. Zhou, J. R. Huang, D. J. Gundlach, T. N. Jackson,"Organic thin-film transistor-driven polymer-dispersed liquid crystal displays on polymeric substrates", *Appl. Phys. Lett.*, vol. 80, pp. 1088–1089, (2002).

3.4 L. Bürgi, T.J. Richards, R.H. Friend, H. Sirringhaus, "Close look at charge carrier injection in polymer field effect transistors", *J. Appl. Phys.*, vol. 94(9), pp. 6129–6137, (2003).

3.5 R. A. Street, A. Salleo, "Contact effects in polymer transistors", *Appl. Phys. Lett.*, vol. 81(15), pp. 2887–2889, (2002).

3.6 B. H. Hamadani, D. Natelson, "Extracting contact effects in organic FETs", *Proc. of the IEEE.*, vol. 93(7), pp. 1306–1311, (2005).

3.7 D. Gundlach, L. Zhou, J. A. Nichols, T. Jackson, P. V. Necliudov, M. Shur, "An experimental study of contact effects in organic thin film transistors", *J. Appl. Phys*., vol. 100(024509), pp. 1–13, (2006).

3.8 O. Marinov, M. J. Deen, B. Iniguez, "Charge Transport in Organic and Polymer Thin-Film Transistors: Recent Issues", *IEE Proc.-Circuits Devices and Syst.*, vol. 152(3), pp. 189–209, (2005).

3.9 Z. Xie, M.S. Abdou, A. Lu, M.J. Deen and S. Holdcroft, "Electrical Characteristics of Poly(3-Hexylthiophene) Thin Film MISFETs", *Can. J. Phys.,* vol. 70, pp. 1171-1177, (1992).

3.10 B. Hamadani, D. Natelson, "Temperature dependent contact resistances in high quality polymer field effect transistors", *Appl. Phys.Lett.,* vol. 84(3), pp. 443–445, (2004).

3.11 K. Ryu, I. Kymissis, V. Bulovic, C. G. Sodini, "Direct Extraction of Mobility in Pentacene OFETs Using C−V and I−V Measurements", *IEEE Electron Device Lett.*, vol. 26, pp. 716–718, (2005).

3.12 B. H. Hamadani, D. Natelson, "Gated nonlinear transport in organic polymer field effect transistors", *J. Appl. Phys.*, vol. 95, pp. 1227–1232, (2004).

3.13 P. V. Necliudov, M. S. Shur, D. J. Gundlach, T. N. Jackson, "Modeling of organic thin film transistors of different designs", *J. Appl. Phys.*, vol. 88, pp. 6594–6597, (2000).

3.14 M. Estrada, I. Mejía, A. Cerdeira, J. Pallares, L.F. Marsal, B. Iñiguez, "Mobility model for compact device modeling of OTFTs made with different materials", *Solid State Electron.*, vol. 52, pp. 787–794, (2008).

3.15 M. C. J. M. Vissenberg, M. Matters, "Theory of the field-effect mobility in amorphous organic transistors", *Phys. Rev. B*, vol. 57(20), pp. 12964–12967, (1998).

3.16 J. C. Scott, G. G. Malliaras, "Charge injection and recombination at the metal-organic interface", *Chem. Phys. Lett.*, vol. 299(1), pp. 115–119, (1999).

3.17 J. Scott, "Metal-organic interface and charge injection in organic electronic devices", *J. Vac. Sci. Technol. A*, vol. 21(3), pp. 521–531, (2003).

3.18 M.A. Baldo, S.R. Forrest, "Interface-limited injection in amorphous organic semiconductors", *Phys. Rev B*, vol. 64(085201), pp. 1–17, (2001).

3.19 Y. Shen, M.W. Klein, D. B. Jacobs, J. C. Scott, G.G. Malliaras, "Mobility-Dependent Charge Injection into an Organic Semiconductor", *Phys. Rev. Lett.*, vol. 86(17), pp. 3867–3870, (2001).

3.20 B.H. Hamadani, D. Natelson, "Nonlinear charge injection in organic field-effect transistors", *J. Appl. Phys.*, vol. 97(064508), pp. 1–7, (2005).

3.21 K. Tsukagoshi, F. Fujimori, T. Minari, T. Miyadera, T. Hamano, Y. Aoyagi, "Supression of short channel effect in organic thin film transistors", *Appl. Phys. Lett.*, vol. 91(113508), pp. 1–3, (2007).

3.22 P. N. Murgatroyd, "Theory of space-charge-limited current enhanced by Frenkel effect", *J. Phys. D.*, vol. 3, pp. 151–156, (1970).

3.23 P. Lara Bullejos, J. A. Jiménez Tejada, M. J. Deen, O. Marinov, W. R. Datars, "Unified model for the injection and transport of charge in organic diodes", *J. Appl. Phys.*, vol. 103(064504), pp. 1–12, (2008).

3.24 M. J. Deen, M. H. Kazemeini, S. Holdcroft, "Contact effects and extraction of intrinsic parameters in poly(3-alkylthiophene) thin film field-effect transistors", *J. Appl. Phys.*, vol. 103(124509), pp. 1–7, (2008).

3.25 I. Kymissis, C. Dimitrakopoulos, S. Purushothaman, "High-Performance Bottom Electrode Organic Thin-Film Transistors", *IEEE Trans. Electron Devices.*, vol. 48, pp. 1060–1064, (2001).

3.26 M. Shur, M. Hack, "Physics of amorphous silicon based alloy field-effect transistors", *J. Appl. Phys.,* vol. 55(10), pp. 3831–3842, (2006).

3.27 V.I. Arkhipov, E. V. Emelianova, Y.H. Tak, H. Bassler, "Charge injection into light emitting diodes: theory and experiment", *J. Appl. Phys.,* vol. 84(2), pp. 848–856, (1998).

3.28 P. Ravirajan, S.A. Haque, D. Poplavskyy, J.R. Durrant, D.D.C. Bradley, J. Nelson, "Nanoporous TiO_2 solar cells sensitised with a fluorene–thiophene copolymer", *Thin Solid Films*, vol. 451−452, pp. 624−629, (2004).

3.29 G. Horowitz, M. E. Hajlaoui, R. Hajlaoui, "Temperature and gate voltage dependence of hole mobility in polycrystalline oligothiophene thin film transistors", *J. Appl. Phys.*, vol. 87, pp. 4456–4463, (2000).

3.30 E. J. Meijer, G. H. Gelinck, E. van Veenendaal, B. H. Huisman, D. M. De Leeuw, T. M. Klapwijk, "Scaling behavior and parasitic series resistance in disordered organic field-effect transistors", *Appl. Phys. Lett.*, vol. 82, pp. 4576–4578, (2003).

3.31 CRC Handbook of Chemistry and Physics (Chemical Rubber Company, Boca Raton, FL, 1997).

3.32 M. J. Deen, M. H. Kazemeini, Y. M. Haddara, J. Yu, G. Vamvounis, S. Holdcroft, and W. Woods, "Electrical Characterization of Polymer-Based FETs Fabricated by Spin-Coating Poly(3-alkylthiophene)s", *IEEE Trans. Electron Devices.,* vol. 51, pp. 1892-1901, (2004).

Chapter 4:
Evaluation of the Charge Density in the Contact Region of Organic Transistors

4.1 Introduction

The present quality level of Organic Thin Film Transistors (OTFTs) [4.1], [4.2] together with refined production techniques like inkjet printing [4.2], have made OTFTs suitable for commercialization. However, it was highlighted in the previous chapter that contact effects limit the performance of state-of-the-art transistors. Also, much attention has been paid by numerous researchers to study the mechanisms that control the injection and transport of charge in the contacts of OTFTs [4.3], [4.4], [4.5], [4.6], [4.7], [4.8]. A clear vision of the distribution of electrical magnitudes along the contacts can help to determine device parameters like threshold voltage [4.9], mobility [4.10], or density of states and traps [4.4]. This information to device designers and technologists will provide the required feedback to improve the device´s performance. A physical model is presented, along with a method to evaluate the density of charge in the contact regions of organic transistors. The evaluation of charge is based on the comparison of experimental current-voltage (*I-V*) and current-temperature (*I-T*) curves with the results of the physical model that links all the different phenomena present in the contacts of OTFTs. The distribution of charge is calculated in different kinds of contacts in OTFTs: contacts that show ohmic and non-ohmic *I-V* responses. In many cases, these different behaviors are treated with different models, such as space-charge-limited transport or injection-limited current models. In our case, we highlight the importance of using a physical model that combines all the phenomena. The physical model used in this

chapter, allows for the interpretation of a wide range of experimental data, including measurements where a single model fails.

This chapter is organized as follows: In section 4.2, we detail the procedure to evaluate the charge density. This procedure is then applied to experimental data taken in transistors with non-ohmic contacts (section 4.3), and in transistors with ohmic contacts (section 4.4). Finally, we present the conclusions of this chapter.

4.2 Procedure to Determine the Charge Density in OTFTs.

In the previous chapter, we mentioned different methods to determine contact effects in OTFTs, such as the analysis of drain current versus drain voltage curves measured at a constant gate voltage [4.3], or by means of scanning probe potentiometry [4.11], [4.12]. In any case, the voltage drop between source and drain, V_{DS}, is shared by a voltage drop in the conducting or intrinsic channel, V'_{DS}, and a voltage drop, V_C, near the contact region of length x_c (see Fig. 3.1). Two resistivity regions are then present along the channel, with two different distributions of charge: the accumulated layer (or intrinsic region) and the contact (or depleted region). Both of them have their own distribution of charge depending on the drain current, I_D, gate voltage, V_G, and the temperature.

The density of charge in the accumulated channel, $\rho_{channel}$, can be estimated as the density of charge per surface unit, σ, divided by the conduction layer thickness, t_{charge}, where σ is given by the field-effect transistor (FET) model [4.13], $\sigma=C_{OX}(V_{GS}-V_T)/e$, C_{OX} is the capacitance of the insulator per unit surface area, V_{GS} is the gate-to-source voltage, V_T is the threshold voltage, and $e=1.6\times10^{-19}$C is the magnitude of the electron charge. We also assume that the conduction layer thickness, t_{charge}, equals the organic

layer thickness, t_o, as reported in [4.4], [4.14]. In addition to the results observed, the conduction layer thickness, t_{charge}, must be comparable to the organic layer thickness, t_o, because otherwise the charge density, $\rho_{channel}=\sigma/t_{charge}$ would produce values close to the molecular density.

The charge density at the contact regions of OTFTs is determined by the comparison of experimental I_D-V_C curves at the contact with calculated ones. The experimental I_D-V_C curves are extracted from I_D-V_{DS} curves of the transistors by means of the techniques detailed in the previous chapter and proposed in [4.5], [4.7], [4.8]. The calculated I_D-V_C curves are based on the physical approach detailed below.

The model used in this chapter gives a more physical approach than the compact model of previous chapter, however, both models consider that the voltage V_C is shared by the voltages associated to the main mechanisms found in a metal-organic contact. The difference between both models is found in the particular I-V relationship for each of the following mechanism: carrier injection through the barrier, $V_{injection}$; barrier lowering associated to image charges [4.12], [4.15] or dipole charge layers at the interface [4.16], V_{red}; and charge drift in the bulk of the contact region, V_{drift}:

$$V_C = V_{injection}(I_D) + V_{red}(I_D) + V_{drift}(I_D). \qquad (4.1)$$

In the compact model proposed in the previous chapter, the link between these three components is the current I_D flowing through the different parts of the structure. The term associated to the barrier lowering is neglected, and the injection term is calculated with an empirical thermionic-emission-like expression which is independent of the drift term.

On the other hand, the physical approach of this chapter evaluates the three terms of (4.1) and they are linked not only by the current I_D, but also by means of the charge density.

Expressions for these effects were already presented in previous chapters. However, here, we briefly recall the relations between the three components in (4.1) with the drain current and charge density in this chapter in (4.3) to (4.6). This review is developed with the aim of a straightforward reading and to explain the steps of the physical approach. This study introduces two kinds of contacts in OTFT, ohmic and non-ohmic. These expressions relate the voltage associated to each physical phenomenon present in the contacts of OTFTs, with the charge density in the different regions of the contacts. Basically, two regions are defined in the contact that give information of the charge density: the metal-organic interface that defines a boundary condition for the charge density, and the bulk (or depleted region) close to it, where the charge is distributed according to drift mechanisms (see again Fig. 3.1).

As mentioned in previous chapters and as reported in the literature [4.5], [4.15], the carriers to be injected from a metal electrode to an organic layer must overcome a barrier which height, φ_M, can be estimated as the difference between the metal work function and the Highest Occupied Molecular Orbital (HOMO) of the organic layer. Typical metal/organic contacts employed in organic transistors produce a large barrier height, see Tables 3.1 and 3.2. This barrier prevents the flow of charge from metal to the organic material and only a saturation current appears,

$$I_{D,sat} = A^* T^2 S e^{\frac{-\varphi_M}{kT}}, \qquad (4.2),$$

where A^*= 120Acm^{-2}K^{-2} is the Richardson´s constant, S is the cross-section of the metal/organic contact, T is the absolute temperature, and k=1.38×10^{-23}J/K is Boltzmann constant. The cross-section of the metal/organic contact, S, is calculated as $S=t_o \times W$, where t_o is the thickness of the organic layer and W is the channel width of the OTFT.

Many experiments show I_D-V_C curves above this saturation limit. A reduced barrier, (φ_M-V_{red}), is a plausible way to interpret experimental data. For a given current I_D above this limit in (4.2), a barrier lowering, V_{red} can be proposed according to:

$$V_{red}(I_D) = V_t(T)\ln\left(\frac{I_D}{A^*T^2Se^{\frac{-\varphi_M}{kT}}}\right), \qquad (4.3)$$

where $V_t(T)\equiv kT/e$ is the thermal voltage.

This expression (4.3) shows that the higher the measured current, I_D, the larger the lowering of the barrier, V_{red}. As explained in previous chapters, the barrier reduction can be justified by the creation of ions near the interfaces by redox reactions. The effect of these ions is the same as the polar molecules which are intentionally introduced to alter the work function of metals [4.16]. The ions formed due to oxidation─reduction processes have a density ρ_{dp} which can be related to the barrier lowering, V_{red}, according to Nernst equation [4.17]:

$$\rho_{dp} = \rho_m e^{\frac{Vred-\Phi}{V_t(T)}}, \qquad (4.4)$$

where ρ_m is the molecular density of the organic material and Φ depends on the materials involved. The link between the interface effects and the drift mechanism in the bulk of the contact is precisely this charge. In a first-order of approximation, the density of free charge carriers at the interface, $p(0)$, is identified to ρ_{dp} ($p(0)=\rho_{dp}$).

The third term in (4.1) is the voltage required for the transport across the contact region. It is calculated assuming that the charge transport is due to the drift of positive charges (we focus on *p*-type OTFTs) in a space-charge region. It is shown in the section 3.2.3 that the voltage drop associated with the charge drift depends on the boundary condition of the charge density at the interface:

$$V_{drift} = \frac{2}{3}\left\{\frac{2J}{\varepsilon\mu}\right\}^{1/2}\left\{\left[x_c + x_p\right]^{\frac{3}{2}} - \left[x_p\right]^{\frac{3}{2}}\right\}, \quad x_p \equiv \frac{J\varepsilon}{2e^2\mu\left[p(0)\right]^2}, \tag{4.5}$$

where the charge is distributed according to

$$p(x) = \frac{p(0)}{\sqrt{1+\frac{x}{x_p}}}, \qquad 0 < x < x_c \tag{4.6}$$

where $J=I_D/S$ is the current density, x_c is the contact length, ε is the permittivity of the organic material, μ is the mobility of the carriers, and the characteristic length x_p defines a point from the contact interface towards the organic film, at which the charge density $p(x_c)$ decays to $p(0)/\sqrt{2}$.

At first sight, (4.5) provides a non-linear I-V_{drift} relation. However, linear I_D-V_C curves can also be interpreted with this formula. As mentioned in chapter 3, linear and non-linear I_D-V_C curves, are particular cases of the (4.5) for limit cases of the characteristic length x_p.

a) If x_p is much smaller than the contact length x_c, then (4.5) is reduced to the classical Mott-Gurney law:

$$I_D \approx \frac{9}{8}\varepsilon\mu S\frac{(V_{drift})^2}{(x_c)^3}. \tag{4.7}$$

b) If the characteristic length x_p is a few times larger than the contact length x_c, then we can expand in Taylor series, $x_p^{3/2}\left\{\left[1+\left(x_c/x_p\right)\right]^{3/2}-1\right\} = 3/2\,x_c x_p^{1/2} + \ldots$, which reduces (4.5) to Ohm´s law:

$$I_D \approx e\,S\,p(0)\,\mu\frac{V_{drift}}{x_c}. \tag{4.8}$$

These asymptotic trends are related to the characteristic length, x_p, which is directly related to the ratio between the current density, J, and the concentration of carriers at the interface, $p(0)$, (see (4.5)). In Fig. 4.1, we present a study of the transition of these two

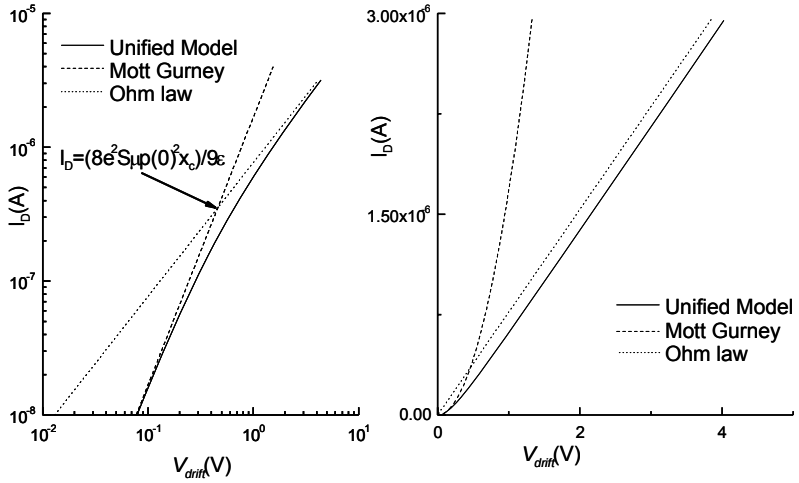

Figure 4.1. Representation of the drift voltage according to (4.5) for currents varying from 0,01μA to 3μA. The parameters of the transistor are: W=270 μm, polymer film t_o=20nm, x_C=100nm, μ=0.12cm^{2}V^{-1}s^{-1} and $p(0)$=10^{16}cm^{-3}. a) log-log scale b) linear scale.

regions for a typical transistor with the following parameters: μ=0.12cm^{2}V^{-1}s^{-1}, W=270 μm, t_o=20nm, x_c=100nm, and ε=3.5ε_o. Fig. 4.1 represents the drain current as a function of the drift voltage according to (4.5) with $p(0)$=10^{16}cm^{-3}. This value is chosen to be consistent with that later in the results section, although any other value could be valid for this theoretical study. In this case, the characteristic length x_p depends only on the current I. For high currents, x_p is also high and the relation I-V_{drift} is linear. For low currents, x_p is low and the relation I-V_{drift} is quadratic. The transition point comes when (4.7) equals (4.8), and it is given in (4.9) for a general case:

$$I_D = \frac{8}{9}\frac{e^2 S\mu p(0)^2 x_c}{\varepsilon}. \tag{4.9}$$

Assuming an experimental value for the drain current, I_D, (4.3) to (4.6) provide the relation between the different terms in (4.1) and the distribution of charge density in the organic material. The calculations of this charge density in different kinds of contacts, is done in the following sections.

The study is made for transistors with the following organic materials: poly(3-hexylthiophene) P3HT or polyfluorene F8T2. Gold and chromium are employed as

source/drain electrodes with the objective of analyzing different barrier heights. The relative permittivity for these organic materials, $\varepsilon_r \approx 3.5$, molecular density, $\rho_m = 2\times10^{21}$ cm^{-3}, electrode work function and the HOMO were given in the previous chapter. The contact length x_c is below 100nm as, deduced by noncontact scanning-probe techniques [4.11], [4.12]. Experimental data used in this study are taken from the literature and, with them, other parameters such as the geometrical dimensions and the mobility in the organic materials.

4.3 Application to Non-Ohmic Contacts.

4.3.1 Extraction of Charge Density from I-V Curves.

Non-ohmic contacts have been detected in Cr/P3HT/Cr OTFTs [4.18]. A non-linear I_D-V_C response of the contact can be extracted, as detailed in previous chapter, from the output characteristics of OTFTs. This procedure is applied here for experimental data taken in Cr/P3HT/Cr OTFTs [4.18]. This is seen in Fig. 4.2a, where the output characteristic at a gate voltage V_G = ─30 V (symbols), its decomposition in the I_D-V_C curve (dashed line) and the I_D-V'_{DS} curve at the intrinsic channel (solid line) are represented.

In Fig. 4.2b, the extracted I_D-V_C curve (crosses) is represented with the results predicted by the physical model (solid line). The three components of the model (V_{red}, circles; V_{drift}, squares; $V_{injection}$, dashed line) are also shown. For a given pair of experimental data (I_D, V_C), the voltages V_{red}, V_{drift}, and $V_{injection}$ are calculated from (4.3), (4.4), (4.5) and (4.1).

The injection voltage is clearly the dominant term; the barrier lowering contributes slightly to the total voltage; and the drift component is also small. The injection barrier in the Cr/P3HT contact is φ_M = 0.5eV. The saturation current,

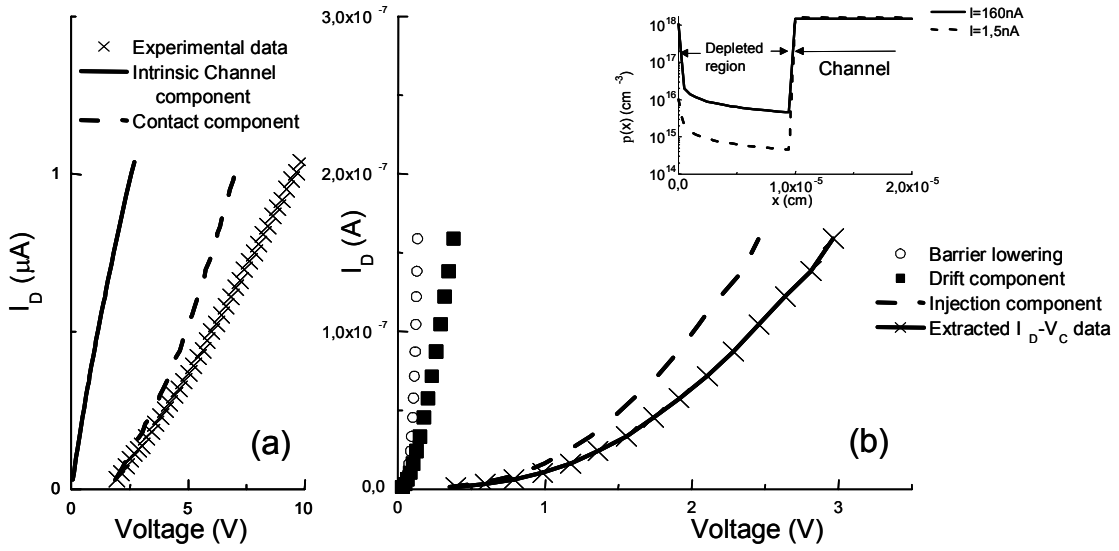

Figure 4.2. (a) Symbols: Transport characteristics of Cr/P3HT/Cr OTFT at 300 K and gate voltage V_G=–30V from [4.18]. L=25μm, W=200μm, SiO_2 thickness 200nm. Organic layer properties: μ=0.13cm^{2}V^{-1}s^{-1} and thickness t_o=20nm. Solid line: Voltage drop along the channel (I_D-V'_{DS}). Dashed line: Voltage drop in the contact (I_D-V_C) (b) Reproduction of the I_D-V_C curve, symbols, with the calculations of the physical model, solid line. The three components of the model (V_{red}, circles; V_{drift}, squares; $V_{injection}$, dashed line) are also shown. The contact width is x_c=100nm, the barrier at the contact between the source and the P3HT is φ_M = 0.5eV and the Cr-P3HT Nernst potential is Φ=0.3V. Inset: Spatial distribution of charge carrier density from source to drain for two different values of the current.

calculated with (4.2) for this barrier, is I_{Dsat}=1nA. That means that a barrier lowering, V_{red}, is needed to allow higher drain currents.

The calculated values for V_{red} are in the range 0.01 to 0.13 V, reducing the natural barrier to a lower value that enhances the current through the contact: (φ_M -V_{red}) is in the range [0.49-0.37] eV and I_D in the range [1nA-160nA].

The I_D-V_C curve shows a quadratic trend which might suggest that we use the Mott-Gurney model. However, a reproduction of the experimental data with Mott-Gurney law alone, would imply the use of an unrealistic contact width x_c=400nm, in comparison with values reported in the literature (x_c<100 nm) [4.11], [4.12]. It is important to highlight that the value of the contact width used in our calculation is in agreement with scanning probe potentiometry results [4.3], [4.12] (x_c=100 nm).

Simultaneously to the determination of the three components of the contact voltage, the distribution of charge can be calculated for any pair of values of (I_D, V_C). The distribution of charge, for two values of the current, is represented in the inset of Fig. 4.2b. As a reference, the density of charge in the accumulated channel of these transistors is $\rho_{channel} \approx 10^{18}\text{cm}^{-3}$ according to MOSFET model [4.13]. The value of the charge density in the depleted region is two orders of magnitude lower than that in the channel. The charge increases towards the interface with the electrode, where it is required to reduce the barrier at the interface. The overall charge in the contact also increases with the current, while the charge in the intrinsic channel is kept fixed at a constant V_G.

The idea of separating the contact voltage into three components was proposed in the previous chapter and published in [4.7]. However, the expressions proposed for these three components in the present chapter have a more physical meaning. In fact, the determination of the charge density in the contact region requires a relation between this charge and the physical mechanisms that occur in the contact region. A comparison between the former compact approach and the one presented in this chapter is seen in Fig. 4.3.

Figure 4.3 shows with crosses, a non-linear I_D-V_C curve extracted for the contacts of Au/Cr-F8T2 OTFTs [4.19]. There are different ways to interpret this non-linear response: A) A thermionic-emission-like expression [4.19], $I_D=I_{Dsat}(\exp(V_C/\eta V_t(\text{T}))-1)$, with high values of the ideality factor η. B) The compact model proposed in previous chapter, which results from the combination of a drift term given by the Mott-Gurney law ($I_D=I_D(V_{drift})$, (3.7)) plus a term associated to the injection through the contacts. This last term can again be described by a simple approach of a thermionic-emission-like expression $I_D=I_{Dsat}(\exp(V_{injection}/\eta V_t(\text{T}))-1)$. In this case, a

lower value for η is necessary in order to reproduce the experimental data, due to the effect of the drift term. This value points out that a more physical approach is closer. And C) the present physical approach that considers a finite value of the charge density at the metal-organic interface, the barrier lowering associated with that charge, and the general expression of the drift term (4.5). The results of approaches B) and C) are compared in Fig. 4.3. The compact and physical approaches (solid and dotted lines,

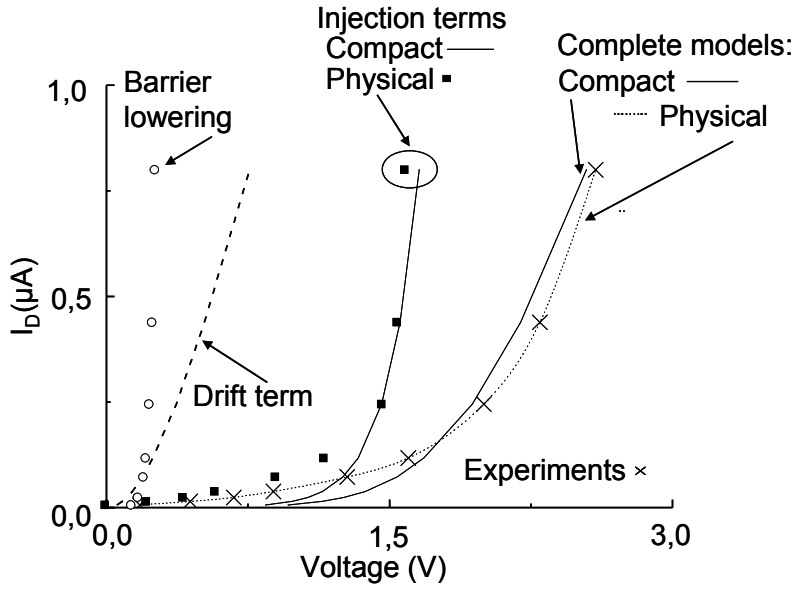

Figure 4.3. Experimental I_D-V_C curves from Au/Cr−F8T2 OTFTs data in [4.19] (crosses), the device parameters are L=5 μm, W=1000 μm, μ=0.006cm^{2}V^{-1}s^{-1}, the SiO_2 gate insulator thickness is 200nm, the metal electrodes are t_O=100nm thick and $V_{GT}=V_{GS}-V_T$=15V. The barrier height is φ_M=0.68eV, and the Nernst potential is Φ=0.4V. The drift term (dashed line) is calculated from (4.7) and a contact width x_C=100nm. The injection term according to the compact model (dotted line) is calculated with a thermionic-emission-like expression [4.19] and the injection according to the physical approach (squares) is calculated with (4.3), (4.4), (4.5) and (4.1). The I_D-V_C curves calculated with the compact model in [4.19] (dotted line), with the physical approach presented in this chapter (solid line) and the experiments (crosses) can be seen on the right of the figure, the compact model fails to reproduce the experiments and the physical model succeeds.

respectively) reproduce the experimental data (crosses). The injection components in both models (closed squares and solid line next to them) are equivalent; and the drift term in both models is coincident (dashed line).

4.3.2 Study with the Temperature.

With the aim of further testing the value of the physical approach presented in this chapter, a study with the temperature is done in this subsection, together with a comparison with other models. Experimental I_D-V_C curves measured at different temperatures in Cr/P3HT/Cr OTFTs [4.18] are represented with symbols in Fig. 4.4a, together with the calculations of our physical approach (solid lines), providing a good agreement. The three components of our model are also represented at these different temperatures (Figs. 4.4a, 4.4b, and 4.4c). Similar dependences with temperature to that of the experimental data are seen in the drift and injection components (Figs. 4.4b, and 4.4c respectively).

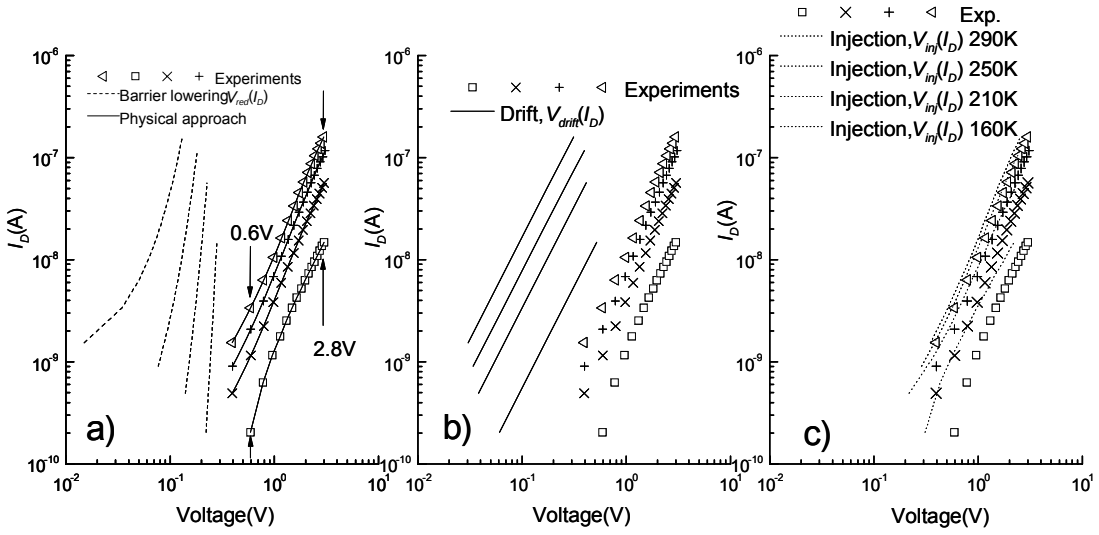

Figure 4.4. Comparison of our calculations at four given temperatures with experimental I_D-V_C curves in Cr/P3HT/Cr OTFT (symbols) [4.18]. (a) Physical approaches (solid lines) along with the voltage associated to the barrier lowering (dashed lines). (b) Voltage associated to the drift (solid lines). (c) Voltage associated to the injection (dotted lines). The parameters used in the physical approach are V_G=–30V, L=25μm, W=200μm, and SiO_2 thickness 200nm. Organic layer properties: ε=3.5, ρ_m=2×10^{21}cm^{-3}, and thickness t_s=20nm. The contact width is x_c=100nm, the barrier at the contact between the source and the P3HT is φ_M = 0.5eV, the Cr-P3HT Nernst potential is Φ=0.32V and μ from [4.18], μ=4×10^{-3}, 24×10^{-3}, 56×10^{-3}, 120×10^{-3} cm^{2}V^{-1}s^{-1} for T=160, 210, 250 and 290K (from bottom to top).

The relatively weak temperature dependence of the experimental I_D-V_C curves is similar to the temperature dependence of the mobility, reported together with the experiments [4.18]. In order to achieve a good agreement between the experimental data

and our results, this temperature-dependent mobility is introduced in our model. This dependence with temperature cannot be explained by injection limited models like thermionic emission [4.18] alone. Only transport models that include a temperature-dependent mobility, plus a temperature-dependent injection, can explain these experiments.

A comparison of our model with other models described in the literature is shown in Fig. 4.5. Experimental I_D-T curves extracted from Fig. 4.4a are used as a reference in this comparison. They correspond to the contact voltages, V_C=0.6 V and V_C=2.8 V. The experimental I_D-T curves at both voltages are represented with symbols in Figs. 5a and 5b respectively.

An injection limited model based on hopping [4.20] succeeds in reproducing the experiments at low contact voltages, but it fails to explain the experiments at high contact voltages (see dashed lines in Fig. 4.5a and Fig. 4.5b respectively). The Mott-Gurney law alone, including with the values for the carrier mobility reported in [4.18], cannot fit the experiments at either low, or at high contact voltages. The results of this model are represented with dotted lines in Fig. 4.5b for two different values of the contact length, x_c.

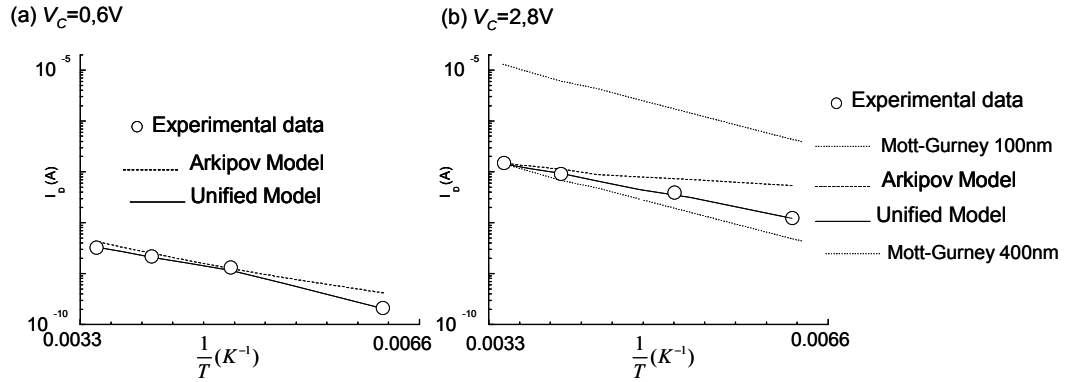

Figure 4.5. (a) Symbols: I_D-T^{-1} curve from Figure 4a at a contact voltage V_C=0.6V. Solid line: prediction of the Unified model. Dashed line: Arkhipov prediction taken from [4.18]. (b) Symbols: I_D-T^{-1} curve from Figure 4a at a contact voltage V_C=2.8V. Solid line: prediction of the Unified model. Dashed line: Arkhipov prediction taken from [4.18]. Dotted line: Mott-Gurney prediction for a contact width x_c=400nm, bottom, and x_c=100nm, top.

A calculation using a contact length x_c =400nm is close to the experimental data. However, a contact width above 100 nm is not realistic, as mentioned earlier [4.12]. The Mott-Gurney law evaluated for a contact length x_c=100nm is also shown in Fig. 4.5b. However, it disagrees with the experimental data, showing that the drift mechanism is not the only one responsible for the contact effects. Only the combination of different physical mechanisms proposed in our approach succeeds in reproducing the experimental data with a realistic value for x_c.

4.4 Application to Ohmic Contacts

4.4.1 Extraction of Charge Density from I-V Curves

The second case to study is an OTFT where the injection barrier between the source contact and the polymer is small. A representative sample of ohmic I_D-V_C responses can be seen in Au/P3HT/Au OTFTs [4.5]. Experimental data taken on these transistors [4.5] are analyzed in this section.

Experimental I_D-V_C curves, at four given gate voltages in Au/P3HT/Au OTFTs [4.5], are represented with symbols in Fig. 4.6a along with the calculations of our physical approach, solid lines. The calculations of the physical model are done as described below.

The injection barrier in the Au/P3HT contact is φ_M=0.28eV as reported in the previous chapter (see tables 3.1 and 3.2) and the saturation current for this barrier, I_{Dsat}=3μA, is above the experimental data. This means that the voltages associated to the barrier lowering and injection are small compared to the drift voltage. In this case, the experimental contact voltage drop V_C can be approximated by the drift voltage, $V_C \approx V_{drift}$ (see (4.1)).

Contact widths, x_c, in ohmic contacts are expected to be smaller than the values reported for non-ohmic: $x_{c(ohmic)} < x_{c(non\ ohmic)} \leq 100$nm. Small values of the contact width x_c result in linear I_D–V_C curves (4.8). Equating the experimental data with (4.8), the distribution of the free charge carriers' density can be obtained for each gate voltage.

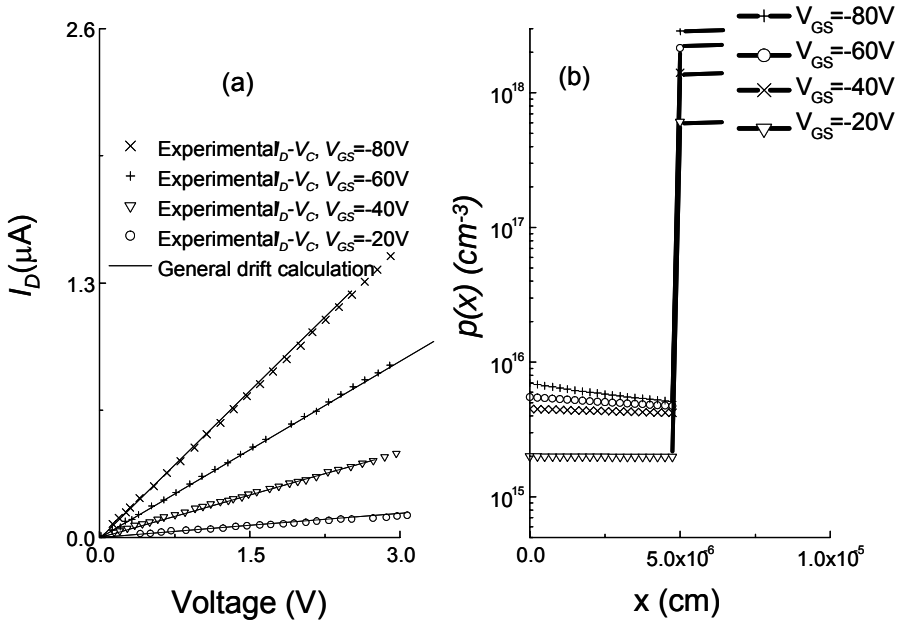

Figure 4.6. a) Symbols: experimental I_c-V_c curves in Au/P3HT/Au OTFT from [4.5] at four gate voltages and T=250K. Solid line: Unified Model prediction with following parameters: L=10μm, W=200μm, SiO_2 thickness: 200nm. Organic layer thickness t_o=30nm, contact width x_c=50nm and mobilities reported in [4.5]. b) Density of charge along the device from source to drain at the gate voltages in (a). The barrier between Gold and P3HT is φ_M= 0.28eV.

Proceeding in this way with experimental data in Fig. 4.6, the distribution of the free charge carriers density is obtained at four different gate voltages (Fig. 4.6b), and increases with gate voltage. The explanation is based on the fact that the charge in the organic layer can be considered free only when it requires a small activation energy to jump to neighbouring sites [4.1], [4.12], [4.21]. When a high gate voltage is applied, charges are attracted to the insulator and they start to fill the traps present in the organic layer, allowing any additional charges to occupy states of high energies which can be considered as free charges. The density of the charge at the interface, $p(0)$, is within the

interval [10^{15}, 10^{16}] cm^{-3} and results in large values of the decay distance x_p. This provides a more uniform distribution of charge than in the case of non-ohmic contacts. The region of low concentration of charge density near the interface is in clear agreement with potentiometry experiments that show a large voltage drop just in this region. The I_D–V_C curves represented in Fig. 4.6a were taken from [4.5] and we can calculate which portion of the drain-source voltage drops in the contact by using (3.5). For the case studied in Fig. 4.6, a 50% of the drain-source voltage drops at the contact.

The main feature of contact effects in Au/P3HT samples is the linearity of the I_D–V_C response. Classical drift models like Mott-Gurney law produces nonlinear I_D–V_C curves because they assume that the density of charge at the interface, $p(0)$, is infinite, see deduction of (4.7) again. Thus, we highlight the importance of a method to evaluate the finite density of charge at the contacts. The determination of the charge density in the contact region of an organic transistor is a step forward towards the determination of charge density in other organic devices, such as organic light-emitting diodes where this evaluation is crucial in order to estimate the recombination rates in the diode.

4.4.2 Study with the Temperature.

In order to gain information about the physical effects that occur inside the depleted region near the contact, a study of the evolution of the charge density with temperature is described below.

Temperature dependent I_D-V_C curves in ohmic contacts can be seen in Au/P3HT/Au OTFTs [4.6]. The I_D-V_C curves measured at three different temperatures [4.6], are represented with symbols in Fig. 4.7a, together with our calculations as solid lines.

The density of charge at the interface can be obtained by equating the experimental contact resistance $R_C = V_C/I_D$, with the slope of (4.8). The mobilities

reported with the experimental data are used in this calculation. The distribution of charge along the contact is represented at three different temperatures in Fig. 4.7b, Fig. 4.7c, and Fig. 4.7d, for two values of the drain current, I_D=0.25μA, and I_D=0.016μA. Similar results are obtained for others currents. An increment of the charge density with the temperature is seen. This means that the free charge density at the contacts increases not only with gate voltage, as seen in previous section, but also with temperature. As explained earlier, the charge in organic materials is considered free when able to hop to neighboring sites, and this hopping process is expected to become easier when the temperature is increased because the charges will have a higher thermal energy.

This increase of charges with temperature shows a parallel behavior to that predicted by other authors on how the charge density in the bulk of the organic film evolves with the temperature [4.3], [4.21]. The decay of the charge density with the distance also varies with the temperature. As mentioned above, the density of charge carriers decays as the square root of the distance according to (4.6). At low temperatures, the density of charge is low enough to make the characteristic distance x_p

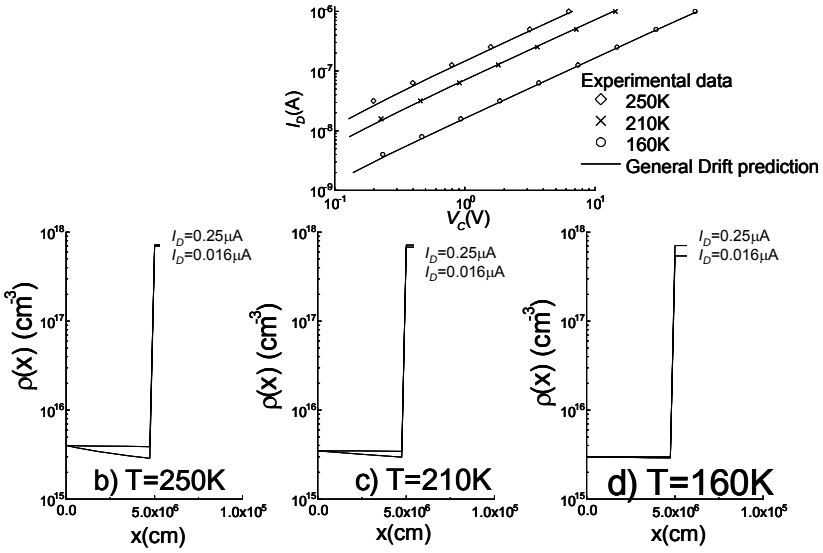

Figure 4.7. (a) Symbols: experimental I_D-V_C curves in Au/P3HT/Au OTFT from the experimental contact resistances reported in [4.6] at three different temperatures and a gate voltage V_G=–60V. Solid lines: Unified Model prediction with parameters in Fig. 4.6 and μ from [4.6], μ=4×10^{-3}, 24×10^{-3}, 120×10^{-3} cm^{2}V^{-1}s^{-1} for T=160, 210 and 250K. (b), (c), and (d) Spatial distribution of the charge carrier density for three different temperatures: (b) T=250K, (c) T=210K, and (d) T=160K.

much higher than the length of the contact region, resulting in a slowly varying density of carriers, as seen in Fig. 4.7d.

4.5 Conclusions

In this chapter, a physical model that allows for the determination of the charge density at the contacts of OTFTs has been presented. This model can also interpret current–voltage and current-temperature measurements at the contacts of OTFTs. Two kinds of contact have been studied: ones introducing non-linear effects in the output characteristics of the transistor and others modeled by a single resistance in series with the channel resistance of the transistor. The interpretation of experimental data in both types of contacts is based, first, on the different energy barrier height of both contacts, and second, on the different distribution of charge density in a low conductivity region close to the contact region. The procedure to determine the distribution of charge density lies on the best fitting of experimental data with the results of our physical model. The calculated charge density at the contacts increases with gate voltage and temperature, similar to reports by other authors, proving the value of the physical approach presented in this chapter. The dimensions of the depletion layer near the contacts used in our model are also in agreement with experimental data.

References

4.1 H. Klauk, G. Schmid, W. Radlik, W. Weber, L. Zhou, C. D. Sheraw, J. A. Nichols and T. N. Jackson, “Contact resistance in organic thin film transistors”, *Solid-State Electron*. Vol. 47, pp. 297-301 (2003).

4.2 H. Klauk, M. Halik, U. Zschieschang, G. Schmid, and W. Radlik, “High-mobility polymer gate dielectric pentacene thin film transistors”, *J. Appl. Phys*., Vol. 92, pp. 5259-5263 (2002).

4.3 M. J. Deen, M. H. Kazemeini, S. Holdcroft, "Contact effects and extraction of intrinsic parameters in poly(3-alkylthiophene) thin film field-effect transistors", *J. Appl. Phys.*, vol. 103(124509), pp. 1–7, (2008).

4.4 K. Tsukagoshi, F. Fujimori, T. Minari, T. Miyadera, T. Hamano, Y. Aoyagi, "Supression of short channel effect in organic thin film transistors", *Appl. Phys. Lett.*, vol. 91(113508), pp. 1–3, (2007).

4.5 B. H. Hamadani, D. Natelson, "Extracting contact effects in organic FETs", *Proc. of the IEEE.*, vol. 93(7), pp. 1306–1311, (2005).

4.6 B. Hamadani, D. Natelson, "Temperature dependent contact resistances in high quality polymer field effect transistors", *Appl. Phys.Lett.,* vol. 84(3), pp. 443–445, (2004).

4.7 P. Lara Bullejos, J. A. Jiménez Tejada, S. Rodríguez-Bolívar, M. J. Deen, and O. Marinov, "Model for the injection of charge through the contacts of organic transistors", *J. Appl. Phys.*, vol. 105(084516), pp. 1–8, (2009).

4.8 P. Lara Bullejos, J. A. Jiménez Tejada, M. J. Deen, and O. Marinov. in Proc. of the 216th ECS Conf. 2009.

4.9 O. Tal, Y. Rosenwaks, Y. Roichman, Y. Preezant, N. Tessler, C. K. Chan, and A. Kahn, "Threshold voltage as a measure of molecular level shift in organic thin film transistors", *Appl. Phys. Lett.,* vol. 88(043509), pp. 1-3 (2006).

4.10 H. Park, D. Shin, H. Yu, and H. Chae, "Electron mobility in tris(8-hydroxyquinoline)aluminum (Alq3) films by transient electroluminescence from single layer organic light emitting diodes", *Appl. Phys. Lett.,* vol. 90(202103), pp. 1-3, (2007).

4.11 K. Seshadri, and C. D. Frisbie, "Potentiometry of an operating organic semiconductor field-effect transistor", *Appl. Phys.Lett.,* vol. 78, pp. 993-995, (2000).

4.12 L. Bürgi, T.J. Richards, R.H. Friend, H. Sirringhaus, "Close look at charge carrier injection in polymer field effect transistors", *J. Appl. Phys.*, vol. 94(9), pp. 6129–6137, (2003).

4.13 S. M. Sze, *Physics of Semiconductor Devices* (Wiley, New York, 1981).

4.14 O. Marinov, M. J. Deen, B. Iniguez, "Charge Transport in Organic and Polymer Thin-Film Transistors: Recent Issues", *IEE Proc.-Circuits Devices and Syst.*, vol. 152(3), pp. 189–209, (2005).

4.15 J. C. Scott, G. G. Malliaras, "Charge injection and recombination at the metal-organic interface", *Chem. Phys. Lett.*, vol. 299(1), pp. 115–119, (1999).

4.16 B. de Boer, A. Hadipour, M. M. Mandoc, T. van Woudenbergh, and P. W. M. Blom, "Tuning of Metal Work Functions with Self-Assembled Monolayers", *Adv. Mater.*, vol. 17, pp. 621-625, (2005).

4.17 P. Lara Bullejos, J. A. Jiménez Tejada, M. J. Deen, O. Marinov, and W. R. Datars, "Unified model for the injection and transport of charge in organic diodes", *J. Appl. Phys.,* vol. 103(064504), pp. 1-12 (2008).

4.18 B.H. Hamadani, D. Natelson, "Nonlinear charge injection in organic field-effect transistors", *J. Appl. Phys.*, vol. 97(064508), pp. 1–7, (2005).

4.19 R. A. Street, A. Salleo, "Contact effects in polymer transistors", *Appl. Phys. Lett.*, vol. 81(15), pp. 2887–2889, (2002).

4.20 V.I. Arkhipov, E. V. Emelianova, Y.H. Tak, H. Bassler, "Charge injection into light emitting diodes: theory and experiment", *J. Appl. Phys.,* vol. 84(2), pp. 848–856, (1998).

4.21 M. C. J. M. Vissenberg, M. Matters, "Theory of the field-effect mobility in amorphous organic transistors", *Phys. Rev. B*, vol. 57(20), pp. 12964-12967 (1998).

Chapter 5:

Conclusions and Future Work

5.1 Conclusions

This thesis presents a physical model that includes several transport mechanisms observed in organic devices. These mechanisms are charge injection (thermionic and FN), charge creation at metal-organic interface, and charge transport through the organic layer (charge drift and space charge effects). Although these mechanisms have been studied before, the inclusion of all of them into a single combined model is new. The combination of physical and chemical mechanisms in our model allows for the interpretation of a wide range of experimental data. The model reproduces experimental data reported in publications from several research groups, including certain measurements that cannot be explained by taking into account only one phenomenon.

The first contribution of this research begins with the theoretical basis of the model, leading to the expressions in the model used to fit the experimental data from previous publications on organic diodes. Key objectives of the proposed equations is the calculation of current-density-voltage (*j-V*) and current-density -temperature (*j-T*) curves. Two important cases have been derived from our model: a low voltage regime,

in which the thermionic injection is dominant, and a high voltage regime, in which the tunnel injection is dominant.

The second contribution concerns a compact model for the charge injection to contacts in OTFTs, which is shown to be very accurate when compared to experimental data. This contribution is very important because charge injection through contacts is often neglected in OTFT models, despite its major impact on the electrical characteristics of OTFTs. A methodology to extract the contact effects using transistors of different channel lengths is presented. Furthermore, in the case when transistors with different channel lengths are not available or the transport depends on the channel length, a new method to extract current voltage curves at the contacts from output characteristics was proposed and verified. This method also allows us to extract the mobility in OTFTs that is impacted by the contact effects. The compact model explains both linear and non-linear current-voltage curves at the contacts of OTFTs. The fitting of various data for nonlinear contacts can help us obtain deeper insights into the details and physical origin of the charge injection in organic devices, simultaneously providing a link to compact modeling.

The third contribution was on modifying the compact model into a more physical one that allows for the determination of the charge density at the contacts of OTFTs. Using this physical model, we have studied the voltage and temperature dependence of the current flowing through these contacts. The study covered two kinds of contact: ones introducing non-linear effects in the output characteristics of the transistor and others modeled by a single resistance in series with the channel resistance of the transistor. The interpretation of experimental data in both types of contacts is based, first, on the different energy barrier height of both contacts, and second, on the distribution of charge density in a low conductivity region close to the contact region. A

method to determine the distribution of charge density at the contacts is proposed. That charge density controls the relation between the different mechanisms that take place near the contacts: thermionic injection across a barrier, and bulk transport in the low conductivity region. It is shown that the contact resistance decreases with the gate bias voltage and temperature, the explanation is found in the fact that the filling of the traps in the defect rich region of the contact allows the increase of free carriers and reduces the contact resistance.

Taken together, these three contributions represent a significant advance in state-of-the-art physical modelling of organic semiconductor devices– from charge creation, to charge injection and finally charge transport in both diodes and thin-film transistors. An important advantage of the proposed models is that they can be incorporated into simulation programs used to design integrated circuits. In this way, the application of organic semiconductor devices may become feasible in transitioning from research labs into commercial products.

5.2 Future Work

The following suggestions for future work, as a continuation and extension of the research described in this thesis is now proposed.

5.2.1 Charge Trapping Effects

It is known that charge trapping (or charge localization) takes a prominent place in amorphous and especially in organic devices, as compared to crystalline semiconductor devices. The effects of charge trapping on the performance of organic devices are several fold. Some of these effects are bias-dependent mobility, threshold shift, hysteresis in electrical and optical characteristics, frequency-time dependences in capacitance-voltage characteristics, gradual-to rapid-degradation of performance parameters impacted by the environmental conditions. Therefore, it would be useful to

investigate these charge trapping effects, which are also known as charge buildup in organic devices.

As a start, published experimental results plus the many phenomenological results in the literature can be used to develop a semi-empirical model for their interpretation. Further, building on published previous experimental results where power-law and stretched-exponential dependences describe the effects related to charge trapping, it will be useful to solve the problem of providing a good physical understanding for the origin of many details in charge-related trapping in organic structures. The solution can initially use an extensive analysis of the trends in existing experimental data in order to find trends relations that will be then converted in models that are both physically plausible and suitable for compact modeling.

Next, the important issues of lifetime and reliability of organic materials and structures that are critical for niche applications such as solar cells or flexible components for disposable electronics should be investigated. Immediate pursuit of this research will be both important and timely because charge trapping effects are to a large extent overlooked by most researchers, since they are classified as unwanted phenomena, whereas these effects would limit the potential advantages of organic devices.

5.2.2 Radiation Effects

Another recommendation for future research is to measure and explain the effect of radiation, for example, Gamma-rays and ion beams on the current-voltage and capacitance-voltage characteristics of organic components, and to determine whether radiation is less damaging than to inorganic devices. To the best of our knowledge, such experiments have not been performed before. It is known that radiation by x-rays, Gamma-rays or ion beams can cause irreversible effects that result in permanent changes in the characteristics of inorganic devices. In metal-oxide-semiconductor field-

effect transistors (MOSFETs), ionization radiation produces electron-hole pairs. In n-type transistors, electrons reach the silicon-silicon dioxide interface. A fraction of these electrons are trapped in the oxide and can last for a long time. This can result in a failure in which there is a shift from an enhancement mode (normally off) to a depletion mode (normally on). The device will be turned on rather than turned off at zero gate voltage. The effects of radiation on organic transistors and diodes may be different from these effects because the conductivity mechanism is different. Probably, electron-hole pairs cannot be produced. Thus, radiation experiments are certainly worthwhile. They can reveal what damage can be done by radiation. The radiation damage will also provide information about charge creation (e.g. excitons) and the conducting mechanism. There is also the chance that very little damage can be done. This would make organic/polymeric devices very useful in applications in which radiation is present. Such innovative research into the investigation of organic/polymeric devices will reveal new insights and show their differences from the properties of inorganic devices. The current-voltage and capacitance-voltage relations of the radiated devices will be measured. The results can be compared with data taken before radiation and data for inorganic devices. The conclusions will provide the models of radiation damage will be developed.

5.2.3 Solar Cells

Solar cells based on organic materials have attracted both academic and industrial interest because of advantages associated to these materials like flexibility, low fabrication costs, weight and low working voltages. The major advantage of organic solar cells is the low cost fabrication which can help to increase the commercialization of photovoltaic devices. To the date, silicon solar cells occupy the main part of the market in photovoltaic devices, but different materials and types of cell

are being investigated to address problems like the high costs and low efficiencies related with the silicon. While reported efficiencies in organic materials are close to fulfilling the requirements for commercial applications, device lifetimes are unsatisfactory. Therefore, the stability is one of the main issues on which efforts should be focused. The main source of degradation is the photo-oxidation of the organic solid, leading to loss in conjugation and irreversible deterioration of the light-absorbing and/or charge-transporting properties. Therefore, it would be useful to investigate materials and fabrication processes which lead to inexpensive and photoelectrically stable solar cells.

As a start, organic solar cells should be characterized and modeled to get deeper insights of the degradation phenomena and which parts of the devices are easier to suffer such processes. The model to develop, should give the distribution of charge and electric field along the solar cell as well as generation rates and the relationship between light flow and induced current. Then, it will be useful to provide a good physical understanding in solar cells with stable fullerenes as solar energy absorbing materials.

Publications During the Doctoral Research

Journal Publications

1. P. Lara Bullejos, J. A. Jiménez Tejada, F. M. Gómez-Campos, M. J. Deen, and O. Marinov, “Evaluation of the charge density in the contact region of organic thin film transistors”, *J. Appl. Phys*., accepted for publication, (2009).
2. P. Lara Bullejos, J. A. Jiménez Tejada, S. Rodríguez-Bolívar, M. J. Deen, and O. Marinov, “Model for the injection of charge through the contacts of organic transistors”, *J. Appl. Phys*., vol. 105 (084516), pp. 1–8, (2009).
3. P. Lara Bullejos, J. A. Jiménez Tejada, M. J. Deen, O. Marinov, and W. R. Datars, “Unified model for the injection and transport of charge in organic diodes”, *J. Appl. Phys*., 103 (064504), 1-12 (2008).
4. J. A. Jiménez Tejada, P. Lara Bullejos, J. A. López Villanueva, F.M. Gómez-Campos, S. Rodríguez-Bolívar, and M. Jamal Deen, “Determination of the concentration of recombination centers in thin asymmetrical p-n junctions from capacitance transient spectroscopy”, *Appl. Phys. Lett*., vol. 89(112107), pp. 1-3, (2006).

Conference Publications

5. **Invited Paper**, P. Lara Bullejos, J. A. Jiménez Tejada, M. J. Deen, and O. Marinov, *Proc. Electrochemical Society Meeting* (216th ECS Meeting) Wien, Austria (2009). In press.
6. P. Lara Bullejos, J. A. Jiménez Tejada, M. J. Deen, O. Marinov, and S. Rodríguez-Bolívar, *IEEE Proc. Spanish Conference on Electron Devices*, Santiago de Compostela, Spain (2009).

7. **Invited Paper** P. Lara Bullejos, J. A. Jiménez Tejada, M. J. Deen, O. Marinov and S. Rodríguez-Bolívar, *Proc*. *International Symposium on Flexible Electronics* (ISFE 08) Tarragona Spain (2008).
8. J. A. Jiménez Tejada, P. Lara Bullejos, and M. J. Deen, *Proc. IEEE International Workshop on Compact Thin-Film Transistor Modeling for Circuit Simulation*, Cambridge U. K. (2008).
9. **Invited Paper** J. A. Jiménez Tejada, P. Lara Bullejos, M. J. Deen, and W. Datars, *Proc. Electrochemical Society Meeting* (212th ECS) Washington DC (2007).
10. J. A. Jiménez Tejada, M. J. Deen, P. Lara Bullejos, J. A. López Villanueva, F.M. Gómez-Campos, and S. Rodríguez-Bolívar, *IEEE Proceeding of the Spanish Conference on Electron Devices*, (2007).